The Astrophysical Journal, 903:34 (20pp), 2020 November 1 https://doi.org/10.3847/1538-4357/abb9a6

Probing the Nature of High-redshift Weak Emission Line Quasars: A Young Quasar with a Starburst Host Galaxy

Irham Taufik Andika[1,2], Knud Jahnke[1], Masafusa Onoue[1], Eduardo Bañados[1], Chiara Mazzucchelli[3], Mladen Novak[1], Anna-Christina Eilers[1,4,10], Bram P. Venemans[1], Jan-Torge Schindler[1], Fabian Walter[1], Marcel Neeleman[1], Robert A. Simcoe[4], Roberto Decarli[5], Emanuele Paolo Farina[6], Victor Marian[1,2], Antonio Pensabene[5,7], Thomas M. Cooper[8], and Alejandra F. Rojas[9]

[1] Max-Planck-Institut für Astronomie, Königstuhl 17, D-69117 Heidelberg, Germany; andika@mpia.de
[2] International Max Planck Research School for Astronomy & Cosmic Physics at the University of Heidelberg, Germany
[3] European Southern Observatory, Alonso de Córdova 3107, Vitacura, Región Metropolitana, Chile
[4] MIT Kavli Institute for Astrophysics and Space Research, 77 Massachusetts Avenue, Cambridge, MA 02139, USA
[5] INAF–Osservatorio di Astrofisica e Scienza dello Spazio di Bologna, Via Gobetti 93/3, I-40129, Bologna, Italy
[6] Max-Planck-Institut für Astrophysik, Karl-Schwarzschild-Straße 1, D-85748, Garching bei München, Germany
[7] Dipartimento di Fisica e Astronomia, Alma Mater Studiorum, Università di Bologna, Via Gobetti 93/2, I-40129 Bologna, Italy
[8] The Observatories of the Carnegie Institution for Science, 813 Santa Barbara Street, Pasadena, CA 91101, USA
[9] Centro de Astronomía (CITEVA), Universidad de Antofagasta, Avenida Angamos 601, Antofagasta, Chile
Received 2020 July 31; revised 2020 September 3; accepted 2020 September 16; published 2020 October 29

Abstract

We present the discovery of PSO J083.8371+11.8482, a weak emission line quasar with extreme star formation rate at $z = 6.3401$. This quasar was selected from Pan-STARRS1, UHS, and unWISE photometric data. Gemini/GNIRS spectroscopy follow-up indicates a Mg II-based black hole mass of $M_{\rm BH} = (2.0^{+0.7}_{-0.4}) \times 10^9\ M_\odot$ and an Eddington ratio of $L_{\rm bol}/L_{\rm Edd} = 0.5^{+0.1}_{-0.2}$, in line with an actively accreting supermassive black hole (SMBH) at $z \gtrsim 6$. Hubble Space Telescope imaging sets strong constraint on lens boosting, showing no relevant effect on the apparent emission. The quasar is also observed as a pure point source with no additional emission component. The broad-line region (BLR) emission is intrinsically weak and not likely caused by an intervening absorber. We found rest-frame equivalent widths of EW (Lyα + N V)$_{\rm rest} = 5.7 \pm 0.7$ Å, EW (C IV)$_{\rm rest} \leqslant 5.8$ Å (3σ upper limit), and EW (Mg II)$_{\rm rest} = 8.7 \pm 0.7$ Å. A small proximity zone size ($R_{\rm p} = 1.2 \pm 0.4$ pMpc) indicates a lifetime of only $t_{\rm Q} = 10^{3.4\pm0.7}$ years from the last quasar phase ignition. ALMA shows extended [C II] emission with a mild velocity gradient. The inferred far-infrared luminosity ($L_{\rm FIR} = (1.2 \pm 0.1) \times 10^{13}\ L_\odot$) is one of the highest among all known quasar hosts at $z \gtrsim 6$. Dust and [C II] emissions put a constraint on the star formation rate of SFR = 900–4900 $M_\odot\ {\rm yr}^{-1}$, similar to that of a hyperluminous infrared galaxy. Considering the observed quasar lifetime and BLR formation timescale, the weak-line profile in the quasar spectrum is most likely caused by a BLR that is not yet fully formed rather than by continuum boosting by gravitational lensing or a soft continuum due to super-Eddington accretion.

Unified Astronomy Thesaurus concepts: Quasars (1319); Supermassive black holes (1663); Active galactic nuclei (16); AGN host galaxies (2017); Intergalactic medium (813); Reionization (1383); Early universe (435)

1. Introduction

Quasars[11] are the most luminous nontransient sources in the universe, and they are very rare, with a number density of only $\lesssim$1 Gpc^{-3} (Inayoshi et al. 2019). Their spectra provide important insights into the properties of the intergalactic medium (IGM) at the later stages of the epoch of reionization (EoR), which is thought to be completed by $z \sim 5.5$ (e.g., Fan et al. 2006; Becker et al. 2015; Mortlock 2016). They are also excellent probes for understanding the build-up of the first supermassive black holes (SMBHs; e.g., Volonteri 2010) as well as the metal enrichment of the first galaxies and of their surroundings (e.g., Chen et al. 2017; Bosman et al. 2017; Maiolino & Mannucci 2019; Onoue et al. 2020). Identification and detailed characterization of more quasars at this epoch will provide us with better constraints on the physical properties of the universe at the end of the transition phase from neutral to ionized hydrogen.

The existence of billion-solar-mass SMBHs at $z \gtrsim 6$ (e.g., Mortlock et al. 2011; Wu et al. 2015; Mazzucchelli et al. 2017; Bañados et al. 2018; Yang et al. 2020) puts stringent constraints on the formation and early growth models of the first SMBHs and host galaxies within the first gigayear after the big bang (see Inayoshi et al. 2019 for a recent review). This challenges standard SMBH formation models, which start from a stellar seed mass black hole that grows via Eddington-limited accretion (e.g., Volonteri 2010, 2012). Among the current theoretical scenarios accounting for the formation of the observed SMBHs are the growth from massive seed black holes ($\gtrsim 10^4\ M_\odot$) through a direct collapse channel (e.g., Begelman et al. 2006; Ferrara et al. 2014; Habouzit et al. 2016; Schauer et al. 2017; Dayal et al. 2019), lower-mass seeds ($\lesssim 10^{2-3}\ M_\odot$) with Eddington-limited or even super-Eddington accretion and very rapid growth (e.g., Ohsuga et al. 2005; Tanaka & Haiman 2009; Inayoshi et al. 2016), or the presence of radiatively inefficient accretion modes (e.g., Trakhtenbrot et al. 2017; Davies et al. 2019). Recent identification of young quasars with estimated lifetimes of only $t_{\rm Q} < 10^4$–10^5 yr at $z \sim 6$ (Eilers et al. 2017, 2018; Davies et al. 2020; Eilers et al. 2020) imposed additional tensions with respect to the standard

[10] NASA Hubble Fellow.
[11] We use the terms "quasar" and "QSO" interchangeably throughout this paper.

growth models of SMBHs. These young quasars are identified based on their small proximity zone, which is the region of enhanced Lyα forest transmission produced by ionizing radiation from the central quasar and before the onset of the Gunn & Peterson (1965) absorption trough (e.g., Eilers et al. 2017).

At lower redshifts ($z \sim 3$–5), a notable group of quasars shows exceptionally weak ultraviolet broad emission lines, originally discovered in the Sloan Digital Sky Survey spectra and systematically investigated by Diamond-Stanic et al. (2009). These so-called weak emission line quasars (WLQs) are defined as having a rest-frame equivalent width of EW (Lyα λ1216 + N v λ1240)$_{\rm rest}$ < 15.4 Å and/or EW (C iv λ1549)$_{\rm rest}$ < 10 Å. Meanwhile, the EW(C iv) of normal quasars follow a log-normal distribution with a mean of $\langle$EW(C iv)$\rangle = 42^{+25}_{-16}$ Å(Diamond-Stanic et al. 2009). Hence, WLQs are the 3σ outliers at the low end of this distribution. Several theories have been proposed to explain the WLQ phenomenon, and according to Plotkin et al. (2015), they fall into two broad categories: (1) soft ionizing continuum theory and (2) anemic broad emission line region (BLR) model. In the soft ionizing continuum idea, one might expect that the BLR is less photoionized so the broad emission lines produced are weak, probably because of (i) inefficient photoionizing photons due to an extremely high accretion rate (Leighly et al. 2007a, 2007b), (ii) low accretion rate in the very massive black hole which leads to a radiatively inefficient cold accretion disk (Laor & Davis 2011), or (iii) high-energy photons produced by the accretion disk are absorbed by shielding materials (Wu et al. 2011; Luo et al. 2015; Ni et al. 2018). On the other hand, the anemic BLR model suggests that the BLR itself could be unusually gas deficient (Shemmer et al. 2010; Nikołajuk & Walter 2012), possibly if the quasar is in an early phase of accretion and the BLR has not yet fully formed (Hryniewicz et al. 2010; Meusinger & Balafkan 2014). It is then critical to study the intrinsic properties of WLQs and the environment of their host galaxies at the highest accessible redshifts to test the evolutionary scenario.

Up to now, there have been around 270 quasars discovered at $z > 6$, mostly found thanks to large-area or deep sky surveys (e.g., Fan et al. 2006; Willott et al. 2010; Mortlock et al. 2011; Venemans et al. 2013, 2015; Bañados et al. 2016; Jiang et al. 2016; Matsuoka et al. 2016, 2018a, 2018b; Mazzucchelli et al. 2017; Reed et al. 2017, 2019; Wang et al. 2017; Pons et al. 2019; Wang et al. 2019; Yang et al. 2019). Among those $z > 6$ quasars discovered, there are only ~20 of them identified as WLQs (Bañados et al. 2016; Shen et al. 2019). To increase the sampling points of reionization at $z > 6$ and to investigate the relationship of rare WLQs and cases of very young quasars, which gives us a handle on early modes of growth, increasing the quasar sample size at this early epoch is critical.

In this paper, we report the discovery of PSO J083.8371 +11.8482 (hereafter PSO J083+11) at $z = 6.34$, as part of our effort to expand the number of known quasars at $z > 6$. In order to investigate the physical properties of this quasar, its host galaxy, and its environment, we performed an extensive, multiwavelength (from optical/near-infrared (NIR) to submillimeter) campaign with state-of-the-art facilities, which we present here. The primary data used for initial candidates selection are outlined in Section 2, while our method for selecting quasars via spectral energy distribution (SED) modeling is described in Section 3. Then, we report the spectroscopic follow-up data in Section 4 to confirm the quasar nature of PSO J083+11 and derive black hole properties. High-resolution Hubble Space Telescope (HST) NIR imaging to test whether gravitational lensing affects the quasar's apparent emission is presented in Section 5. After that, in Section 6, the proximity zone size and quasar lifetime calculations are presented. The host galaxy properties from submillimeter observation based on the Atacama Large Millimeter/submillimeter Array (ALMA) are explored in Section 7. Section 8 discusses possible physical processes that drive the weakness of PSO J083+11 BLR emission. We close by summarizing the paper and its conclusions in Section 9.

We use AB zero points for all magnitudes written in this paper. We further assume a flat ΛCDM cosmology with $\Omega_{\rm m} = 0.3$, $\Omega_\Lambda = 0.7$, and $H_0 = 70$ km s^{-1} Mpc^{-1} for all physical measurements. Using this assumption, at $z = 6.3401$, the age of the universe is 0.852 Gyr, and an angular scale of $\theta = 1''$ corresponds to a proper transverse separation of 5.6 kpc.

2. Initial Candidate Selection from Public Multiband Data

Our quasar candidate selection is a two-part process: (1) preselection of candidates from multiband photometric data and (2) modeling of the SED to derive relative probabilities for a candidate to be a quasar or contaminant.

We started the first part of our quasar search by exploiting the Pan-STARRS1 survey, following and expanding the selection by Mazzucchelli et al. (2017) to focus on the redshift range $6.3 \leqslant z \leqslant 7.1$. Then, we added various infrared photometric data points from public surveys to help us classify and estimate the photometric redshift of each candidate. The catalog photometry was corrected for Galactic reddening by using the `Bayestar19` dust map (Green et al. 2019) and the Fitzpatrick (1999) reddening law. Then, we cross-matched with a list of late -M stars along with L and T dwarfs (hereafter MLT dwarfs) from Best et al. (2018) and quasars from Flesch (2019) to exclude those known objects from our list of $z > 6$ quasar candidates. Finally, we carried out follow-up spectroscopy of promising targets as the final confirmation of their nature. We will provide the technical details for each step in the following section.

2.1. Main Optical Catalog

We use the Pan-STARRS1 catalog internal release version (PS1 version 3.4; Chambers et al. 2016) as the main data for the initial quasar candidate selection. The 5σ limiting magnitudes of this stack catalog are $g = 23.3$, $r = 23.2$, $i = 23.1$, $z = 22.3$, $y = 21.3$. Due to intervening intergalactic medium (IGM), the $z \gtrsim 6.2$ quasar's flux on the blue side of Lyα is expected to be heavily absorbed, creating a strong break in the flux. This will also make them basically undetected, i.e., have very low signal-to-noise ratios (S/Ns), in all bands bluer than the z band at the PS1 limiting magnitude. For the selection, we require candidates to be detected in the PS1 y band and have very red colors. In summary, the criteria used are

$$\mathrm{S/N}(g_{\rm PS1},\ r_{\rm PS1},\ i_{\rm PS1}) < 8 \quad (1)$$

$$\mathrm{S/N}(y_{\rm PS1}) > 7 \quad (2)$$

$$\mathrm{S/N}(z_{\rm PS1}) \geqslant 3 \text{ and } z_{\rm PS1} - y_{\rm PS1} > 1.2 \quad (3)$$

$$\text{or}$$

$$\mathrm{S/N}(z_{\rm PS1}) < 3 \text{ and } z_{\rm PS1,lim} - y_{\rm PS1} > 1.2$$
$$y_{\rm PS1} > 15 \quad (4)$$

where all measured fluxes and magnitudes are based on point-spread function (PSF) photometry, unless stated otherwise. The magnitude limit criterion in Equation (4) is used to exclude unusually bright objects or spurious sources.

However, quasars of extreme brightness could still be detected in some PS1 "dropout" bands. This might be because of their intrinsically high luminosity (e.g., Wu et al. 2015) or their apparent fluxes are boosted by gravitational lensing events (e.g., Fan et al. 2019; Fujimoto et al. 2020). Moreover, most strongly lensed quasars would be removed as candidates due to Equation (1) because the massive lensing galaxy at intermediate redshift would contribute flux in those bands. Hence, additional criterion is applied if Equation (1) is not fulfilled to actually find this population:

$$(g_{\rm PS1},\ r_{\rm PS1},\ i_{\rm PS1}) - y_{\rm PS1} > 3.0. \quad (5)$$

There are some useful parameters in the PS1 catalog that can be utilized to remove most of the contaminants. The first one is to exclude objects showing extended morphology and only choose point like or very compact sources by requiring

$$|y_{\rm PS1,aper} - y_{\rm PS1}| < 0.5, \quad (6)$$

where $y_{\rm PS1,aper}$ and $y_{\rm PS1}$ are the PS1 catalog aperture and PSF magnitudes of stacked images, respectively. This cutoff threshold was chosen based on tests of spectroscopically confirmed galaxies and stars, following Bañados et al. (2016). Second, the measured PSF magnitudes also need to be consistent with each other:

$$|y_{\rm PS1,stk} - y_{\rm PS1,wrp}| < 0.5, \quad (7)$$

where "stk" and "wrp" denote photometry from stacked images and the mean photometry of single-epoch images, respectively. Lastly, the expected weighted PSF flux is required to be located in good pixels to a percentage of 85% or more, i.e., PSF_QF > 0.85 in the catalog. By using the aforementioned criteria, we obtained ∼17 million candidates at the preliminary selection step (see Table 1).

Some areas of PS1 are also covered by the Dark Energy Spectroscopic Instrument Legacy Imaging Surveys Data Release 8 (DELS; Dey et al. 2019) and the Dark Energy Survey Data Release 1 (DES; Abbott et al. 2018). The advantages of DELS and DES are that they reach magnitude levels ∼1 mag fainter compared to PS1. DELS[12] is conducted using imaging data from three different telescopes, covering ∼14,000 deg^2 of extragalactic sky visible from the northern hemisphere ($-18° <$ decl.$< +84°$) in three optical bands. These data reach 5σ depths of $g = 24.0$, $r = 23.4$, and $z = 22.5$ mag (Dey et al. 2019). On the southern hemisphere, DES[13] is utilizing the Dark Energy Camera mounted on the Cerro Tololo Interamerican Observatory 4 m Blanco telescope to image ∼5000 deg^2 of the southern Galactic cap region in five broad bands. The median coadded catalog depth for a 1.″95 diameter aperture at S/N = 10 is $g = 24.33$, $r = 24.08$, $i = 23.44$, $z = 22.69$, and $Y = 21.44$ mag (Abbott et al. 2018). Hence, the DELS and DES catalogs are cross-matched to our main PS1 catalog with 2″ radius and we will use their photometric data if available.

Selecting high-redshift ("high-z," $z \gtrsim 6$) quasar candidates through the color criteria becomes complicated due to contamination from other populations: late-M stars along with L and T dwarfs (MLT dwarfs) and elliptical galaxies at $z = 1$–2 (hereafter ellipticals). These populations have a higher surface density than the target high-z quasars themselves but have similar NIR colors. Hence, to reduce the number of MLT dwarfs contaminating the candidate sample, we exclude the sky region around M31 ($7° <$ R.A. $<14°$; $37° <$ decl. $< 43°$) and the Milky Way plane ($|b| < 20°$). However, with the advantage of the `Bayestar19` (Green et al. 2019) dust maps, we include some candidates in the Galactic plane region if they have reddening of $E(B-V) < 1$ in the selection, as a difference from previous studies that rigorously excluded all regions with $E(B-V) > 0.3$ (e.g., Bañados et al. 2016; Mazzucchelli et al. 2017).

To make a more refined and more robust selection, we need to take advantage of infrared photometry, because it will give us a parameter dimension to distinguish quasars from MLT dwarfs and ellipticals.

Table 1
Summary of Quasar Selections

Step	Selection	Candidates	Known Quasars
1	Initial query with:		
	PSF_QF > 0.85		
	S/N ($y_{\rm PS1}$) $\geqslant 5$		
	$y_{\rm PS1} > 15$		
	$z_{\rm PS1} - y_{\rm PS1} > 1.0$		
	Excluding Galactic plane		
	Excluding M31	17170000	27
2	Detection in NIR or MIR	5631392	27
3	S/N($y_{\rm PS1}$) $\geqslant 7$	3627100	27
4	$\lvert y_{\rm PS1,aper} - y_{\rm PS1}\rvert < 0.5$	1158750	24
5	$\lvert y_{\rm PS1,stk} - y_{\rm PS1,wrp}\rvert < 0.5$	1059373	24
6	$z_{\rm PS1} - y_{\rm PS1} > 1.2$	367190	22
7	S/N ($g_{\rm PS1}$, $r_{\rm PS1}$, $i_{\rm PS1}$) < 8, or		
	($g_{\rm PS1}$, $r_{\rm PS1}$, $i_{\rm PS1}$) $- y_{\rm PS1} > 3$	74374	22
8	SED fitting	7808	20
9	Forced photometry	1263	20
10	Visual inspection	155	20

Note. Each selection step shows the number of candidates and recovered known quasars at $z > 6$. Our method is most sensitive to select quasars at $6.3 \leqslant z \leqslant 7.1$ due to step 1 requirements.

2.2. Public Infrared Data

We take advantage of public surveys when their sky footprint overlapped with that of PS1. In this case, NIR photometry for the northern hemisphere was taken from the UKIRT Infrared Deep Sky Survey DR10 (UKIDSS; Lawrence et al. 2007) and the UKIRT Hemisphere Survey DR1 (UHS; Dye et al. 2018), while in the southern hemisphere, we used the Vista Hemisphere Survey DR6 (VHS; McMahon et al. 2013) with a 2″ cross-matching radius. The J- as well as H- and K-band magnitudes are very useful to discriminate between quasars and MLT dwarfs (Mazzucchelli et al. 2017; Yang et al. 2019; Wang et al. 2019). This is also an efficient method to remove spurious sources like cosmic rays that are usually only detected in one survey and not in the others.

In addition, mid-infrared (MIR) data were taken from the unWISE catalog (Schlafly et al. 2019), which contains roughly

[12] http://legacysurvey.org/
[13] https://www.darkenergysurvey.org/

two billion objects, observed by the Wide-field Infrared Survey Explorer (WISE; Wright et al. 2010) over the whole sky. The $W1$ (3.4 μm) and $W2$ (4.6 μm) of WISE photometric bands are useful to separate quasars from MLT dwarfs (e.g., the $W1 - W2$ color). The advantage of unWISE compared to the original WISE catalog (AllWISE) is significantly deeper imaging data and improved source extraction in crowded regions (Schlafly et al. 2019). A 3″ cross-match radius to our main catalog was applied. By default, we defined that a source is detected in the NIR/MIR if the catalog entry of the corresponding flux measurements is not empty, i.e., there is a match within the cross-matching radius.

3. Quasar Search via Spectral Energy Distribution Modeling

The second part of our selection method is our own implementation of fitting the full available SED to templates of quasars and the main contaminants to fully exploit the multiwavelength data. The end result of this procedure is to estimate both the photometric redshift and the probability of each source being a quasar or contaminant.

We used all MLT dwarf spectra observed by Burgasser (2014), which are stored in the SpeX Prism Library.[14] This contains ∼360 templates that represent typical M5–M9, L0–L9, and T0–T8 stars. By default, the covered wavelength interval is 0.65–2.55 μm (from $i_{\rm PS1}$- to K-band). To extend the template into the MIR region covered by the WISE data, we calculate the corresponding $W1$ (3.4 μm) and $W2$ (4.6 μm) magnitudes, following Skrzypek et al. (2015), who derived color relations in MLT dwarfs with photometric and spectral data. Following Mazzucchelli et al. (2017), we derive the unWISE magnitudes using the synthetic K-band magnitude and factors for scaling (K_W1 and $W1\_W2$) for each MLT dwarf template, depending on the spectral type. The following equations were applied:

$$W1 = K - K\_W1 - 0.783, \tag{8}$$

$$W2 = W1 - W1\_W2 - 0.63. \tag{9}$$

The quasar models were taken from several observed composite spectra that were derived either from low- or high-redshift quasars spectra. Our first template comes from Selsing et al. (2016), who build a luminous quasar composite spectrum at $1 < z < 2$ selected from SDSS. They performed spectroscopic observation with VLT/X-Shooter to cover ultraviolet to NIR wavelength simultaneously. This approach ensures that the full rest-frame wavelength range from Lyβ to 11350 Å is covered by the composite spectrum with very low contamination from host galaxy stellar emission. The second template is from Jensen et al. (2016), who utilized 58,656 Baryon Oscillation Spectroscopic Survey (BOSS) quasar spectra at $2.1 \leqslant z \leqslant 3.5$ and created the composite binned by redshift, spectral index, and luminosity. The third template that we used was constructed by Harris et al. (2016), which is the averaged spectra of 102,150 BOSS quasars located at $2.1 < z < 3.5$.

Three composites of $z > 5.6$ quasar spectra were constructed by Bañados et al. (2016). The first one is the averaged spectra of ∼100 sources, the second is built by including only the top 10% objects by strongest rest-frame Lyα+NV equivalent width, and the third was constructed by using the 10% sources with the smallest Lyα+NV EW. These different templates allow us to see how changes due to Lyα emission line strength variation affect the quasar color. To reconstruct the intrinsic quasar spectra before absorption of the intervening IGM, we correct each Bañados et al. (2016) quasar template using the prescription from Inoue et al. (2014) as calculated at redshift $z = z_{\rm median}$ of the quasars used to create the composite.

Note that the three composite spectra from Bañados et al. (2016), one from Jensen et al. (2016), and one from Harris et al. (2016) only cover up to a rest-frame wavelength of ∼1500 Å. So, we extended those templates' coverage by stitching them to the template from Selsing et al. (2016) redward of this wavelength. Then, we account for internal reddening by applying the Calzetti et al. (2000) dust model. Levels of reddening are varied from $E(B - V) = 0$ to 0.14 with a 0.02 increment, in addition to two negative reddenings of −0.01 and −0.02 to model the quasars with a bluer continuum than covered by the templates.

For completeness, we also make use of the Brown et al. (2014) atlas of galaxy SEDs. These 129 galaxy SED templates include various galaxy types like spirals, ellipticals, and starburst, which are derived from nearby ($z \lesssim 0.05$) galaxy observation. Internal reddening was accounted for by applying the Calzetti et al. (2000) dust model to the templates with $A(V) = 0$ to 1 with 0.2 increments. Then, we make a grid of models by shifting all the galaxy templates over the redshift interval $0.0 \leqslant z \leqslant 3.0$ with $\Delta z = 0.005$. However, we only use these templates in visual inspection as a final step to make sure that our high-z quasar candidates do not resemble a $z < 6$ galaxy SED.

The SED fitting was done by using the EAZY photometric redshift software, created by Brammer et al. (2008). The way EAZY works is by stepping through a grid of redshifts and trying to find the best template. Here we consider the redshift interval of $4.0 \leqslant z \leqslant 8.0$ with $\Delta z = 0.003$ for the quasar SED models. Template spectra are corrected for intervening H I cloud absorption following the prescription from Inoue et al. (2014). The template fit properly treats flux errors and negative flux measurements because it is done in linear space. The solutions with the smallest reduced χ^2 ($\chi^2_{\rm red}$) are chosen as best-fit models, which can be computed for each template i as

$$\chi^2_{i,\rm red} = \sum_{n=1}^{N} \left(\frac{\rm data_n - f_n(model_i)}{\sigma(\rm data_n)} \right)^2 \Big/ (N-1) \tag{10}$$

where the number of photometric data points is N and the degree of freedom is $(N - 1)$.

Photometric redshifts ($z_{\rm phot}$) may systematically be off from spectroscopic redshifts ($z_{\rm spec}$), and we define this as systematic offset bias (see, e.g., Carrasco Kind & Brunner 2013; Nishizawa et al. 2020). This bias can be calculated as $\Delta z = (z_{\rm phot} - z_{\rm spec})/(1 + z_{\rm spec})$. In our quasar candidate selection, we keep track of how many known quasars we can recover at each step (see Table 1). For the sample of 22 known $z > 6$ quasars on which we run our SED code on, the average bias is $\langle \Delta z \rangle = 0.01$, the scatter is $\sigma_{\Delta z} = 0.02$, and the outlier fraction is $|\Delta z| > 0.15 = 0\%$. Although this represents substantial scatter in the photo-z accuracy, this is already enough to separate between low- and high-z quasars. Note that our method is most sensitive to select quasars at $6.3 \leqslant z \leqslant 7.1$ due to our initial color cut criterion (see step 1 in Table 1). From a total of ∼130 known quasars in this redshift range, there are only ∼30 quasars that were originally discovered within the PS1 and DELS data. The other $\gtrsim$100 quasars are found from deeper surveys like

[14] http://pono.ucsd.edu/~adam/browndwarfs/spexprism/library.html.

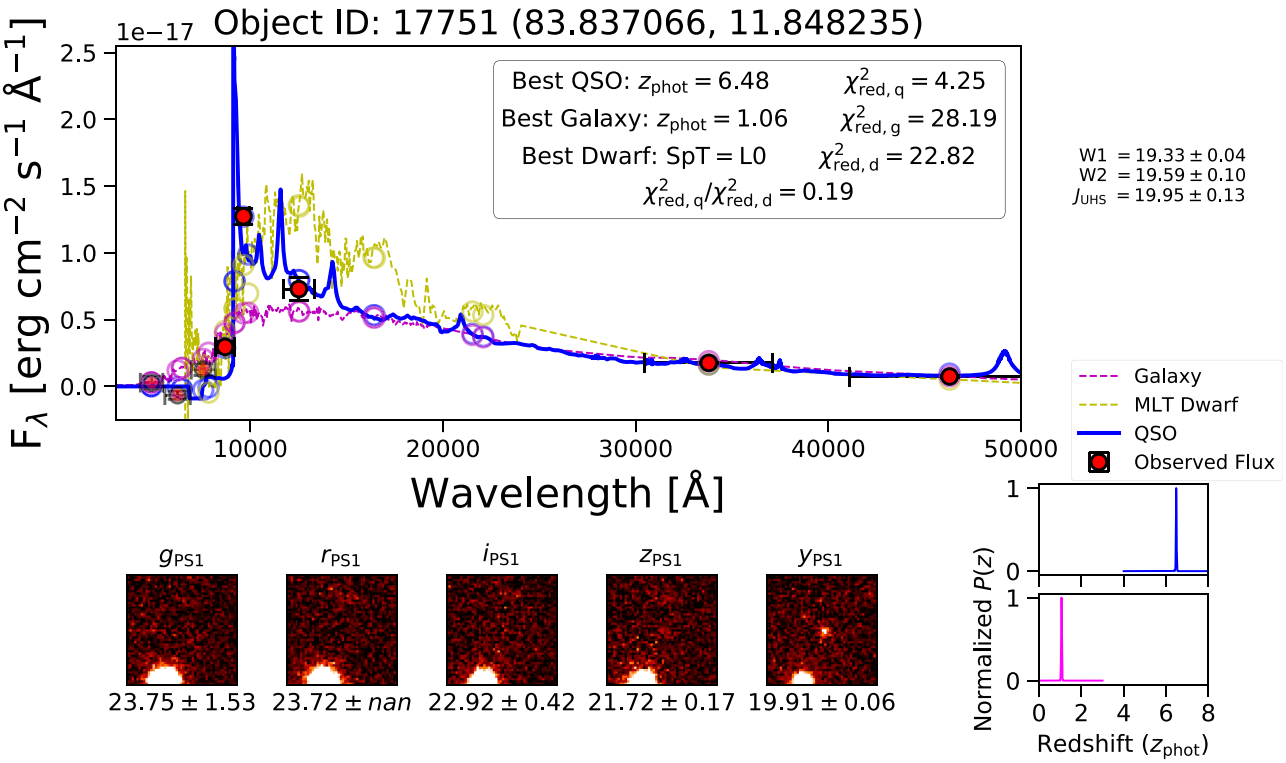

Figure 1. SED fitting result for PSO J083+11. Photometry data are shown with red filled circles with error bars in the top panel. The best-fit quasar spectral template is shown with the blue line and blue circles for model photometry. The same goes for galaxy (magenta) and MLT dwarf models (yellow). The bottom panels show 12″ cutouts in the five PS1 bandpasses. All written magnitudes are corrected for Galactic extinction. Finally, the bottom-right panel shows the probability density function (PDF) of the calculated photo-z's for quasar (blue line) and galaxy (magenta line) models.

SHELLQs, CFHQS, or outside PS1 footprints (e.g., DES, VIKING).

The most-probable high-z quasar candidates are selected based on the χ^2_{red} of the quasar ($\chi^2_{red,q}$) and MLT dwarf ($\chi^2_{red,d}$) model fit, in addition to the estimated photometric redshift (photo-z). The ratio of the two χ^2_{red} ($\chi^2_{red,q}/\chi^2_{red,d}$) is also used as an important factor because this represents how more likely the candidate is a quasar (q) compared to being an MLT dwarf (d). The best values to discriminate between quasars and MLT dwarfs are empirically derived by modeling the SEDs of known PS1 quasars (see the compilation in Flesch 2019) and Best et al. (2018) MLT dwarfs. An example of the SED fitting results can be seen in Figure 1. We choose to use the following criterion:

$$\frac{\chi^2_{red,q}}{\chi^2_{red,d}} < 0.35 \quad (11)$$

which rejects 89% of the potential contaminants while recovering 91% of the known quasars and leaves us with the remaining 7808 candidates.

As an additional step, we performed forced photometry on the remaining candidates to confirm the measurements from the catalog and remove spurious detections (see Bañados et al. 2014, 2016 for reference). For each candidate, the algorithm computed a 2″ radius aperture photometry on the 1′ × 1′ stacked images[15] centered on the candidate's coordinate. It is expected that the aperture photometry is noisier than the PSF photometry. Hence, we imposed a criterion that our own magnitude measurements from the stacked images to be consistent within 2σ compared to the magnitudes in the PS1 catalog. After that, the measured photometry needs to fulfill Equations (1)–(5), leaving us with 1263 candidates.

Finally, visual inspection was done of all the single-epoch and stacked images of PS1 and other public survey, when available. This is a final step to discard non-astronomical sources (e.g., CCD artifacts, moving objects, hot pixels). After that, the 155 surviving candidates were included in our list for NIR spectroscopic follow-up observation. A summary of our selection steps can be found in Table 1.

4. Spectroscopic Observations and Analysis

To confirm the quasar nature of our targets, we performed several spectroscopic campaigns. As of 2020 July, seven promising candidates have been spectroscopically observed. Five of them are identified as contaminants while the other two, PSO J083.8371+11.8482 and PSO J344.1442–02.7664, are previously unknown $z > 6$ quasars. The spectroscopically rejected candidates are reported in Appendix A while the discovery of PSO J344.1442–02.7664 is reported in Appendix B. We followed up PSO J083.8371+11.8482 with deeper NIR spectroscopy, which we will discuss in the following.

4.1. Initial Classification and Redshift Determination with Magellan/FIRE

We first confirmed PSO J083.8371+11.8482 (hereafter PSO J083+11) as a quasar at $z \sim 6.3$ via low-resolution NIR spectroscopic follow-up by using 6.5 m Magellan/FIRE (Simcoe et al. 2013) on 2018 December 31 with a total integration time on target of only 5 minutes. The observation

[15] The PS1 stacked images can be retrieved with `panstamps` (see https://panstamps.readthedocs.io/en/latest/index.html).

was done using the high-throughput prism mode with a slit width of 0.″6, resulting in a spectral resolution of $R = 500$. The observed wavelength range covered by this instrument is $\lambda_{\rm obs} \sim 0.82$–$2.51$ μm.

A second observing run to take a substantially deeper NIR spectrum of PSO J083+11 was done in January and February 2019, using the same telescope. The quasar was observed for 5 hr in the high-resolution echellette mode with the 0.″6 slit. This in principle gives us $R = 6000$ spectral resolution or around $\sim$50 km s^{-1} velocity resolution in the wavelength range of 0.82–2.51 μm. Unfortunately, this second observation run suffered from suboptimal condition, which degraded the S/N. Still, a quick look at the spectra showed that all key emission lines—e.g., Lyα λ 1216, C IV λ 1549, and Mg II λ 2798—appear unexpectedly weak. We modeled the emission lines and continuum despite the noisy spectrum and found that its continuum power-law slope is consistent with a Type 1 quasar located at $z = 6.34$. We have to note that the region around Mg II is heavily affected by telluric absorption, which made the accurate line measurement difficult. To mitigate this issue and to reduce instrument-specific effects, we carried out another spectroscopic observing run.

4.2. Near-infrared Spectroscopy with Gemini/GNIRS

We obtained deep NIR spectroscopy with Gemini Near-InfraRed Spectrograph (GNIRS) at the 8.1 m Gemini North telescope (GN-2019A-FT-204, PI: M. Onoue) on 2019 March 20–22 with a total integration time on target of 8060 s. The runs were executed in the cross-dispersed mode to cover the observed wavelength range $\lambda_{\rm obs} \sim 0.9$–$2.5$ μm, corresponding to $\lambda_{\rm rest} \sim 1200 - 3400$ Å in the rest frame. We utilized the "short" camera with a resolution of 0.″15 per pixel and a 31.7 l/mm grating. We used a slit with aperture of 0.″675, resulting in a spectral resolution of $R \sim 750$. The exposure time for single frame was set to 155 s, and a standard ABBA offset pattern was applied between exposures to better remove the contribution from the sky emission. The airmass range of the observations was $\sim$1.1–1.7.

Data reduction was performed with `PypeIt`,[16] an open-source spectroscopic data reduction pipeline (Prochaska et al. 2020). Each exposure was bias-subtracted and flat-fielded using standard procedures. The wavelength solution was obtained by comparing the spectrum of the sky with the prominent OH (Rousselot et al. 2000) and water lines.[17] After removing contamination from cosmic rays, the pipeline optimally subtracts the background by modeling the sky emission with a *b*-spline function that follows the curvature of the spectrum on the detector. The 1D spectrum of the quasar was created for each exposure using optimal weighting (Kelson 2003). Relative flux calibration was performed with A-type stars observed before or after the target exposures. We used `Molecfit`[18] (Kausch et al. 2015; Smette et al. 2015) to do telluric absorption correction, after which single-exposure one-dimensional spectra were coadded. All 1D spectra were coadded and scaled to the observed UHS *J*-band photometry ($J_{\rm UHS} = 20.09 \pm 0.13$, not corrected for Galactic extinction) for absolute flux calibration. The reddening due to Galactic extinction is then corrected by using the dust map from Green et al. (2019) and the extinction law from Gordon et al. (2016). Figure 2 shows the final spectrum in rest frame. From now on, we will use the GNIRS spectrum for the primary analysis instead of the FIRE spectrum, unless otherwise stated explicitly.

4.3. Modeling the Emission Lines and Underlying Continuum

To model the PSO J083+11 spectrum, we used a multi-component fitting approach. The global continuum was modeled using combined power-law and UV Fe II templates (Vestergaard & Wilkes 2001; Tsuzuki et al. 2006; Salviander et al. 2007). Free parameters are the scaling factor for each component and the power-law continuum slope. We implemented this approach by using a modified version of `PyQSOFit`,[19] a code to fit typical quasar spectra (Guo et al. 2018). We improved the performance of `PyQSOFit` with respect to high-z quasars by optimizing the fit of the narrow and broad emission lines, substituting the continuum windows and other minor modifications. We define the continuum window for the fit by iteratively marking emission- and telluric-line-free regions. The following wavelength ranges were selected as continuum windows: $\lambda_{\rm rest} =$ 1285–1290 Å, 1315–1325 Å, 1350–1370 Å, 1445–1465 Å, 1580–1650 Å, 2140–2300 Å, 2340–2400 Å, 2420–2480 Å, 2630–2710 Å, 2745–2765 Å, and 2850–3000 Å.

The rest-frame 1450 Å absolute magnitude and the monochromatic luminosity at 3000 Å (L_λ(3000 Å)) were calculated from the best-fit power-law continuum. Then, the bolometric luminosity $L_{\rm bol}$ was derived using the empirical correction from Richards et al. (2006):

$$L_{\rm bol} = 5.15 \times \lambda L_{3000}. \quad (12)$$

After subtracting the best-fit continuum and scaled iron templates, each broad emission line was modeled with single Gaussian functions. We applied Monte Carlo simulations and created mock spectra to estimate the errors of the derived parameters. Random flux density errors are drawn assuming a normal distribution using the noise spectrum then applied to the raw spectrum with 1000 iterations. The measurement lower and upper-limit values are taken as the 16th and 84th percentiles of the distribution of these repeated measurements, respectively. Finally, we obtained the equivalent width (EW), central wavelength, FWHM, and velocity dispersion for each line.

However, as seen in Figure 2, the only strongly detected broad line is Mg II, where we found FWHM (Mg II) = 4140^{+880}_{-430} km s^{-1} and EW (Mg II)$_{\rm rest} = 8.71^{+0.67}_{-0.64}$ Å. Moreover, we obtained the redshift of $z_{\rm Mg\,II} = 6.346 \pm 0.001$, determined from the observed Mg II central wavelength. The Lyα is weak, and we do not significantly detect the C IV line. The derivation of the Lyα and C IV EWs will be explained later in Section 6. Assuming that C IV will have an FWHM similar to or larger than that of Mg II, we do not see any potential broad absorption-line signatures in the region where C IV is expected to be present (see the bottom panel of Figure 2). Hence, we conclude that the absence of C IV is not simply caused by the broad absorption-line phenomenon, but rather by the actual nature of this quasar (see Section 6).

[16] https://pypeit.readthedocs.io/en/latest/
[17] https://hitran.org
[18] https://www.eso.org/sci/software/pipelines/skytools/molecfit
[19] https://github.com/legolason/PyQSOFit.

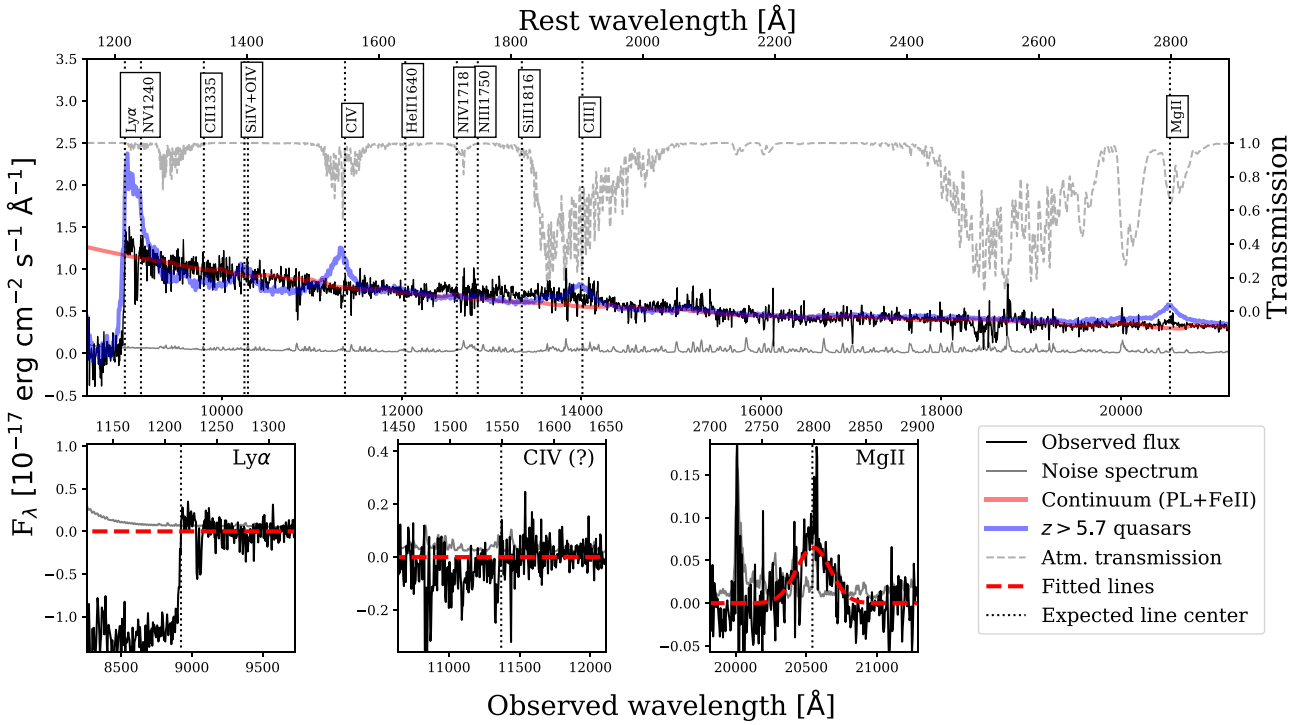

Figure 2. Upper panel: the spectrum of PSO J083+11 taken with Gemini/GNIRS. The observed flux (black), noise (gray), scaled atmospheric transmission (dashed gray, unit in the right axis), and continuum, which consists of a power law plus Fe II emission (red) are shown. The expected emission line centers are shown by the black vertical dotted lines. For comparison, the median composite spectrum of quasars at $z > 5.7$ taken from Shen et al. (2019) is plotted in blue. The Shen et al. (2019) composite spectrum is scaled by taking the median of the PSO J083+11 continuum flux at $\lambda_{\rm rest} = 1300$–$2000$ Å so those two spectra are matched with each other. Lower panel: the continuum-subtracted spectrum around the key emission lines (black) and best-fit Gaussian models (dashed red). Note the sharp emission at the center of Mg II is caused by imperfect telluric correction, so it is not real. We also detect a possible metal absorber near the Lyα emission, at $\lambda_{\rm obs} = 9037$ and 9066 Å.

4.4. Black Hole Mass and Eddington Ratio

The mass of the black hole is derived from our single-epoch NIR spectra. With the assumption that the virial theorem is valid for the BLR dynamics, we use the scaling relation for the Mg II line from Vestergaard & Osmer (2009):

$$\frac{M_{\rm BH}}{M_\odot} = 10^{6.86}\left(\frac{\rm FWHM(Mg\ II)}{10^3\ {\rm km\ s^{-1}}}\right)^2\left(\frac{\lambda L_\lambda(3000\ {\rm Å})}{10^{44}\ {\rm erg\ s^{-1}}}\right)^{0.5} \quad (13)$$

where $\lambda L_\lambda(3000\ {\rm Å})$ is the rest-frame luminosity at 3000 Å and FWHM(Mg II) is the Mg II FWHM. Then, we calculated the Eddington luminosity as

$$L_{\rm Edd} = 1.3 \times 10^{38}\left(\frac{M_{\rm BH}}{M_\odot}\right)\ {\rm erg\ s^{-1}}. \quad (14)$$

After that, we can derive the Eddington ratio as $L_{\rm bol}/L_{\rm Edd}$. We obtained a black hole mass of $\log(M_{\rm BH}/M_\odot) = 9.30^{+0.16}_{-0.10}$ and normalized accretion rate of $L_{\rm bol}/L_{\rm Edd} = 0.51^{+0.13}_{-0.17}$ for the GNIRS spectrum. As a comparison, we derived $\log(M_{\rm BH}/M_\odot) = 9.06^{+0.24}_{-0.16}$ and $L_{\rm bol}/L_{\rm Edd} = 0.77^{+0.33}_{-0.33}$ from the combined FIRE spectra. We report the error in measured virial black hole mass, which we calculated by propagating monochromatic luminosity errors and Mg II line width. However, please note that we did not explicitly add systematic errors, which tend to be larger (≈0.5 dex) compared to random measurement errors (Vestergaard & Osmer 2009; Shen 2013).

In order to compare PSO J083+11 properties to other quasars at high redshifts, we compile Mg II line-width and continuum luminosity measurements for ∼70 previously published $z > 5.7$ quasars (Jiang et al. 2007; Willott et al. 2010; De Rosa et al. 2011, 2014; Wu et al. 2015; Mazzucchelli et al. 2017; Eilers et al. 2018; Fan et al. 2019; Onoue et al. 2019; Shen et al. 2019; Tang et al. 2019). Then, we classify five quasars with EW (C IV) < 10 Å in Shen et al. (2019) as high-z WLQs. On the other hand, 261 WLQs at $z \sim 1.3$ are taken from Meusinger & Balafkan (2014). We use their Mg II line-width and continuum measurements to derive bolometric luminosities and virial masses with the same cosmology assumption and scaling relation (see Equations (12) and (13)) as those applied for PSO J083+11. Figure 3 shows the distribution of calculated parameters in the black hole mass–bolometric luminosity plane. Our object populates the same $L_{\rm bol}/L_{\rm Edd}$ and $M_{\rm BH}$ parameter space as other quasars at $z > 5.7$ and those observed at $z \sim 2$ from SDSS Data Release 7. Hence, we find that PSO J083+11 is powered by a typical mature and actively accreting SMBH, which has been reported in other quasars at similar luminosity ranges. A summary of calculated physical parameters is shown in Table 2.

5. Searching for a Lensing Galaxy

It is well known that gravitational lensing can potentially boost a quasar's observed flux, which could lead to a substantial overestimation of the powering black hole masses. This would have an impact on our understanding of a high-z quasar's intrinsic properties. Furthermore, a large intrinsic lensing fraction among luminous high-z quasars has been predicted (Comerford et al. 2002; Wyithe & Loeb 2002). Moreover, Pacucci & Loeb (2019) predicted that there should be many mildly magnified ($\mu \leqslant 10$)

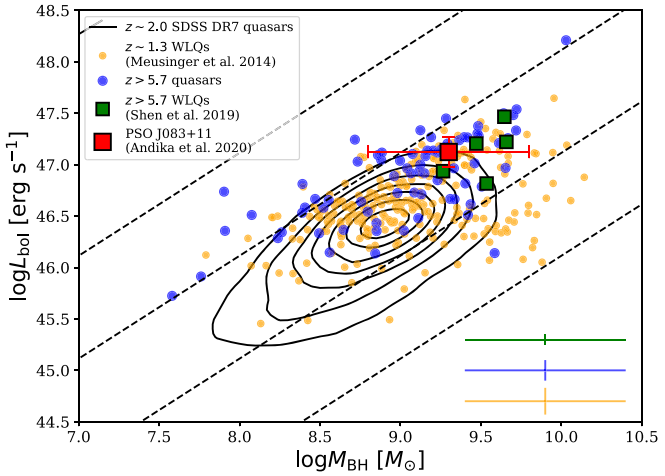

Figure 3. The black hole mass–bolometric luminosity plane of quasars at various redshifts. Those parameters are calculated for a sample of $z \sim 1.3$ WLQs (magenta; Meusinger & Balafkan 2014), $z > 5.7$ WLQs (green; Shen et al. 2019), and other $z > 5.7$ quasars compiled from literature (blue; see text for details). The 0.5 dex systematic uncertainty associated with the Mg II-based black hole mass estimate (Shen 2013) and the measurement errors are taken into account in the error bars (red square with error bars). Contours show the distribution of the $z \sim 2$ SDSS DR7 quasars (Shen et al. 2011). The diagonal lines show Eddington ratios of $L_{\rm bol}/L_{\rm Edd} =$ 10, 1, 0.1, and 0.01 from top left to bottom right. The associated typical uncertainties for each sample are shown as error bars in the bottom right.

quasars at $z > 6$ with extremely small image separation ($\Delta\theta \lesssim 0\farcs2$). The first confirmation of this prediction is the lensed quasar at $z = 6.51$ found by Fan et al. (2019), J043947.08 +163415.7. While there is no obvious companion in the vicinity of PSO J083+11 as judged from the discovery images, the ground-based seeing prohibits detecting various potential lens configurations with small separations. Hence, we have used the Hubble Space Telescope (HST) to test the lensing hypothesis for this quasar.

5.1. Near-infrared Imaging with HST

We obtained high-resolution imaging for PSO J083+11 by using HST (GO 15707, PI: K. Jahnke). Our goal is to test the quasar image being subject to gravitational lensing by utilizing two methods. The first one is by searching for multiple quasar images using the NIR F125W filter ($\lambda_{\rm eff} = 12365$ Å) on the Wide Field Camera 3 (WFC3). The second one is directly searching for an intervening galaxy with the Advanced Camera for Surveys (ACS) ramp filter FR853N ($\lambda_{\rm eff} = 8528$ Å) in the quasar Gunn–Peterson absorption trough just shortward of Lyα, where the quasar light will be nearly fully absorbed, maximizing visibility of any intervening lensing galaxy. Each band was exposed for two orbits, for a total integration time of ~80 minutes per filter. For the WFC3/IR imaging, we rotated the field between the two orbits by ~15°, to analyze not only the images directly, but also the difference image that reduced the interference of instrumental point-source spikes integral to the HST PSF. Data reduction was carried out with the HST pipeline for a final image pixel scale of $0\farcs128$ pixel^{-1}. The 5σ surface brightness limit for a 1 arcsec^2 aperture is ~26 mag arcsec^{-2}.

Our next step is to analyze the WFC3/F125W HST image and search for extended emission, which could be due to an intervening lensing galaxy, companion source, or the host galaxy of PSO J083+11 itself. Our approach is to remove the point-like emission from the central quasar, utilizing the `Photutils`[20] software (Bradley et al. 2019). We chose eight stars in the field to construct a PSF using median-averaging. The stars are chosen so that they are sufficiently away from the edge of the CCD or potential contaminants. They also have to be 1.5×–15× brighter than the quasar to get accurate PSF wings. Note that we did not take into account the effect of the spectral types of selected reference stars; hence, there might be color-dependent uncertainties due to systematic SED differences. Then, this model is fitted to the quasar's nuclear emission in the image, allowing the PSF centroid to move by less than a pixel. The observed image and PSF subtraction residual are shown in Figure 4.

Table 2
Derived Physical Parameters of PSO J083+11

Parameter	Value	Unit
α_λ	$-1.66^{+0.01}_{-0.04}$	
M_{1450}	-26.67 ± 0.01	mag
$M_{\rm BH}$	$(2.00^{+0.74}_{-0.44}) \times 10^9$	$M_\odot$
$L_{\rm bol}$	$(1.33^{+0.01}_{-0.03}) \times 10^{47}$	erg s^{-1}
$L_{\rm bol}/L_{\rm Edd}$	$0.51^{+0.13}_{-0.17}$	
FWHM (Mg II)	4140^{+880}_{-430}	km s^{-1}
Δv(Mg II − [C II])[a]	237 ± 150	km s^{-1}
EW (Mg II)$_{\rm rest}$	$8.71^{+0.67}_{-0.64}$	Å
EW (Lyα + N V)$_{\rm rest}$	$5.65^{+0.72}_{-0.66}$	Å
EW (C IV)$_{\rm rest}$[b]	$\leqslant 5.83$	Å
R_p	1.17 ± 0.32	pMpc
$t_{\rm Q}$	$10^{3.4\pm0.7}$	yr
$z_{\rm [C\ II]}$	6.3401 ± 0.0004	
FWHM ([C II])	229 ± 5	km s^{-1}
Flux ([C II])	10.22 ± 0.35	Jy km s^{-1}
$S_{244\ \rm GHz}$	5.10 ± 0.15	mJy
$S_{258\ \rm GHz}$	5.54 ± 0.16	mJy
$L_{\rm [C\ II]}$	$(1.04 \pm 0.04) \times 10^{10}$	$L_\odot$
$L_{\rm FIR}$	$(1.22 \pm 0.07) \times 10^{13}$	$L_\odot$
$L_{\rm TIR}$	$(1.72 \pm 0.09) \times 10^{13}$	$L_\odot$
SFR$_{\rm [C\ II]}$	800–4900	$M_\odot$ yr^{-1}
SFR$_{\rm TIR}$	900–7600	$M_\odot$ yr^{-1}
$M_{\rm dust}$	$(4.88 \pm 0.14) \times 10^8$	$M_\odot$

Notes.
[a] Velocity shift of Mg II with respect to [C II].
[b] This is the 3σ upper-limit value; see Section 6.

5.2. Modeling a Possible Gravitational Lensing Effect

We identified emission in the WFC3/F125W images, which could be attributed to an intervening foreground galaxy having a potential gravitational lensing effect, located at 1″ to the southwest from the central quasar. However, we could not constrain a redshift of this emission by using HST data only. Its AB magnitude was estimated using aperture photometry, with an aperture of 4 pixel (~0.″5) radius with a value of mag$_{\rm F125W} = 25.42 \pm 0.07$. However, this emission does not show up in the ACS/FR853N image. We did the photometry with the same aperture size and obtained a 5σ upper-limit magnitude of mag$_{\rm FR853N} = 23.25$.

[20] https://photutils.readthedocs.io/en/stable/

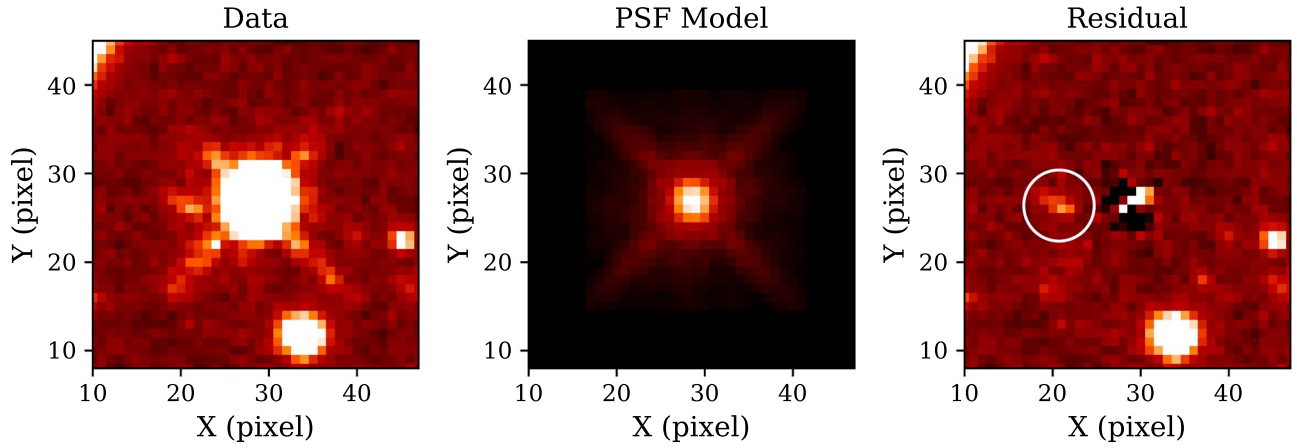

Figure 4. HST WFC3/IR F125W imaging of PSO J083+11. The observed quasar emission (left), PSF model (middle), and the PSF-subtracted image (right) are shown. The image pixel scale is $0\farcs128$ pixel^{-1}. The white circle in the residual image marks the aperture used to determine the aperture photometry of the (likely) foreground galaxy, located $\sim 1''$ from the central quasar. We use a 4 pixel radius aperture (equivalent to $\sim 0\farcs5$) to get an F125W band magnitude $= 25.42 \pm 0.07$.

We test whether the intervening galaxy could potentially boost the apparent quasar emission by modeling the galaxy's emission from the far-ultraviolet to the microwave regimes using BAGPIPES[21] (Carnall et al. 2018). We used the measured flux from WFC3/F125W image aperture photometry, complemented with upper-limit fluxes from the ACS/FR853N and PS1 bands as input data. Here, we assume the foreground emission, which was found in the F125W images to be from a star-forming main-sequence galaxy. To derive the stellar mass and star formation rate (SFR), we need to scale the galaxy SED by choosing a particular star formation history (SFH) model. The simplest form of a parametric model uses up to three shape parameters and a normalization. The most simple and widely used parametric SFH model is exponentially declining (tau model, τ). For this work, we consider the delayed exponentially declining SFHs, which is a tau model multiplied by the time since star formation began (T_0). This would remove both a discontinuity in SFR at T_0 and models with rising SFHs if τ is large (see Carnall et al. 2018). The model will fit the total formed stellar mass and time since star formation began with uniform priors in the value ranges of $M_{\rm formed} = 10^{1-15} M_\odot$ and $T_0 = 0.5 - 0.8$ Gyr, respectively. We assume a fixed value for the SFR timescale ($\tau = 0.3$ Gyr), the metallicity ($Z = 0.02$; equals to solar metallicity), and the nebular emission parameter ($\log(U) = -3$). The value of $A_V = 1.0$ mag was also applied following the Calzetti et al. (2000) extinction law.

For us, the central output calculated by BAGPIPES is the redshift-dependent galaxy stellar mass, which we will use to constrain the possible magnification for PSO J083+11 by applying the lensing equation (see Schneider 2006 for a review). Given the upper limit for the mass-to-light ratio ($\sim$100) for disk and ellipticals, we can estimate the maximum total lens mass, including the dark matter contribution, from the galaxy stellar mass output of the model. Assuming a point-mass gravitational lens configuration, the possible combinations of Einstein angle ($\theta_{\rm E}$) and magnification (μ) can be calculated. Given the calculated lensing galaxy masses, we find limits of $\theta_{\rm E} \leqslant 0\farcs5$ and $\mu \leqslant 1.07$. Therefore, strong magnification of the quasar's emission by the foreground galaxy can be excluded. The calculated Einstein angles as a function of simulated galaxy masses and redshifts are shown in Figure 5.

[21] https://github.com/ACCarnall/bagpipes

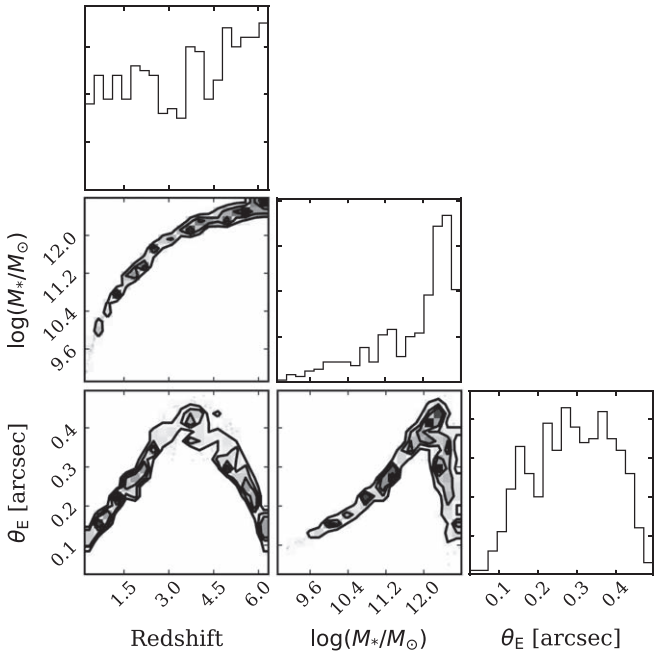

Figure 5. A corner plot showing the calculated Einstein angles as a function of simulated galaxy masses and redshifts.

6. Weak Emission Lines and Young Quasar Accretion Lifetime

As already noted in Section 4.3, the quasar broad emission lines are very weak or absent. We follow the prescription by Diamond-Stanic et al. (2009) to determine the Lyα+N V equivalent width, where the fluxes above the power-law continuum in the range of 1160–1290 Å were integrated. This region is dominated by blended Lyα λ 1216 and N V λ 1240 components, although there is also a small fraction of S III λ 1263. The calculated Lyα+N V equivalent width is EW (Lyα + N V)$_{\rm rest} = 5.65^{+0.72}_{-0.66}$ Å. In addition, we applied the same procedure for the wavelength range of 1500–1600 Å to estimate the 3σ upper limit of the C IV λ 1549 equivalent width, for which we find EW (C IV)$_{\rm rest} \leqslant$ 5.83 Å. From these measurements, we can classify PSO J083+11 as a weak-line quasar according to the empirical definition of

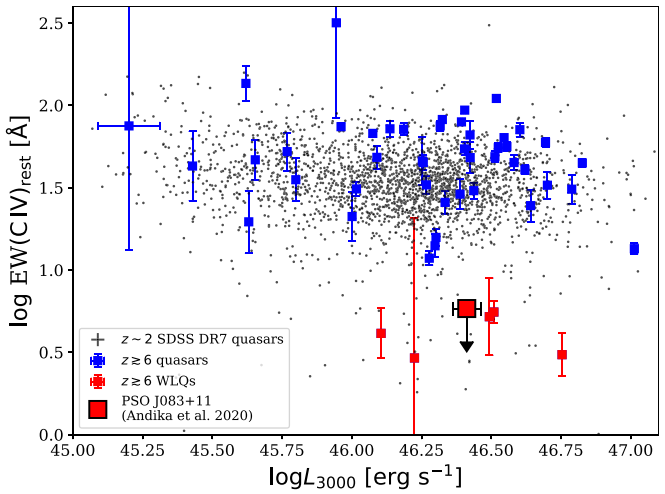

Figure 6. The C IV rest-frame EW as a function of continuum luminosity at 3000 Å. The black dots show the sample of $z\sim2$ quasars from Shen et al. (2011). The $z>5.7$ normal quasars (blue squares) and WLQs (red squares) taken from Shen et al. (2019) are also shown. It is clear that PSO J083+11 is the 3σ outlier at the low end of the normal quasars' EW (C IV)$_{rest}$ log-normal distribution.

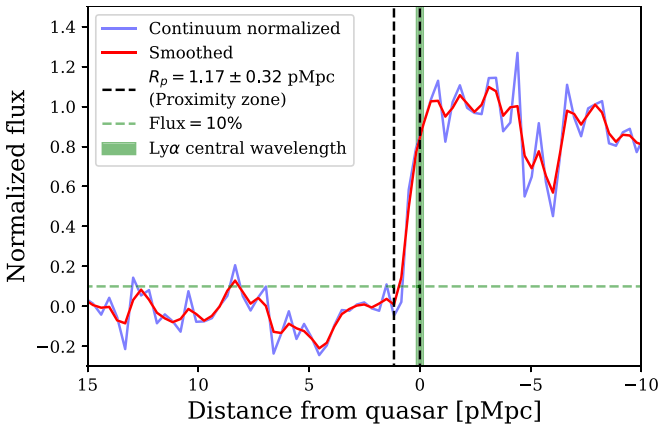

Figure 7. Measured proximity zone size (R_p) of PSO J083+11, marked with two black dashed lines. The expected position of the Lyα central wavelength is marked with green line. Continuum-normalized and smoothed spectra are shown as blue and red lines, respectively. Here we observe a rather small proximity zone of $R_p = 1.17 \pm 0.32$ pMpc.

Diamond-Stanic et al. (2009). The comparison between normal quasars and the WLQs' EW (C IV)$_{rest}$ as a function of continuum luminosity is shown in Figure 6. Although originally WLQs are defined as quasars having EW (C IV)$_{rest}$ <10 and found in low-redshift ("low-z," $z\lesssim5$) quasars, this definition is still valid for high-z quasars. Shen et al. (2019) showed that there is no significant redshift evolution of EW (C IV)$_{rest}$, at least up to $z\sim6$ (see their Figure 8).

Eilers et al. (2017) showed that the lifetime of quasars can be inferred from their proximity zone sizes. By definition, the proximity zone is the region of enhanced Lyα forest transmission close to the quasar resulting from its own ionizing radiation. The IGM will have a finite response time to reach a new ionization equilibrium state due to the quasars' radiation with a timescale of $t_{eq}\approx\Gamma_{\rm H\,I}^{-1}\approx3\times10^4$ yr. Here, $\Gamma_{\rm H\,I}$ is the rate of photoionization (Eilers et al. 2017).

In practice, we continuum-normalized the quasar Magellan/FIRE spectrum and applied a convolution with a 20 Å resolution boxcar kernel. Then, the proximity zone size is defined as the distance from the center of Lyα to shorter wavelengths where the transmitted flux first drops below 10% of the level at the line (Fan et al. 2006). Note that this is done in the observed frame of the wavelength. The result is shown in Figure 7. The conversion of the proximity zone size to the quasar lifetime can be inferred from radiative transfer simulations (Davies et al. 2016) for quasars with similar redshift and luminosity to our quasar and is shown in the Figure 8. We observe a rather small proximity zone ($R_p=1.17\pm0.32$ pMpc) in the spectrum, which implies that PSO J083+11 has a lifetime of only $t_Q=10^{3.4\pm0.7}$ yr. As a comparison, the typical proximity zone sizes of quasars with $-27.5\lesssim M_{1450}\lesssim-26.5$ are $R_p=3-7$ pMpc while their typical lifetimes are $t_Q=10^{5-6}$ yr (Eilers et al. 2017).

7. Probing the Quasar Host Galaxy

7.1. Submillimeter Observation with ALMA

The ALMA band-6 observations were performed to spatially resolve the [C II] 158 μm line, determine an accurate redshift, and investigate the host galaxy of PSO J083+11 (2019.1.01436.S, PI: I. T. Andika). We integrated for a total on-source time of 3145 s with observation carried out on 2019 October 9 using ALMA's C43-4 array configuration. The receivers were set to cover ~258 GHz, which is the expected [C II] frequency ($\nu_{rest}=1900.5369$ GHz) at $z=6.34$ (see Section 4.2).

The data set was calibrated with a pipeline implemented in Common Astronomy Software Application[22] (CASA; McMullin et al. 2007). Next, the TCLEAN task was applied using natural weighting to image the visibilities while maximizing the point-source sensitivity. We focused on a 5″ circular region around the central quasar and performed the cleaning down to 2σ. Then, we masked out the line-containing channels and used a simple median approximation to model the continuum. After that, we produced continuum-free data by subtracting the continuum model from visibilities. The final imaged cubes have a 30 MHz channel width, a synthesized beam of around $0\farcs42\times0\farcs37$, and an rms noise level of ~0.24 mJy beam^{-1}.

7.2. [C II] Spectral Profile

The [C II] spectrum is extracted with an aperture radius of 1.″5 (equivalent to 8.3 kpc) to maximize the recoverable emission. We chose this value because there is no further [C II] flux recovered outside this radius. Ill-defined units make the flux measurement in interferometric maps challenging (see Novak et al. 2019 for further details). Assume that we have the aperture fluxes measured inside the dirty image D, the clean component C only, and the residual image R. Then, the scaling factor for corrections is $\epsilon=C/(D-R)$. The most important factors that govern the scaling factor ϵ are the clean and dirty beam sizes. In our case, $\epsilon\approx0.6$. Then, we use the dirty image flux and multiply it with ϵ to get the final flux density in proper units. Note that if using the final image only to measure the flux, we would obtain ~10% larger values. This happens because the final image is a superposition of clean Gaussian components plus residuals. The extracted spectrum is shown in Figure 9, and a Gaussian fit results in the integrated [C II] line flux of 10.22 ± 0.35 Jy km s^{-1}, FWHM of 229 ± 5 km s^{-1},

[22] https://casa.nrao.edu/

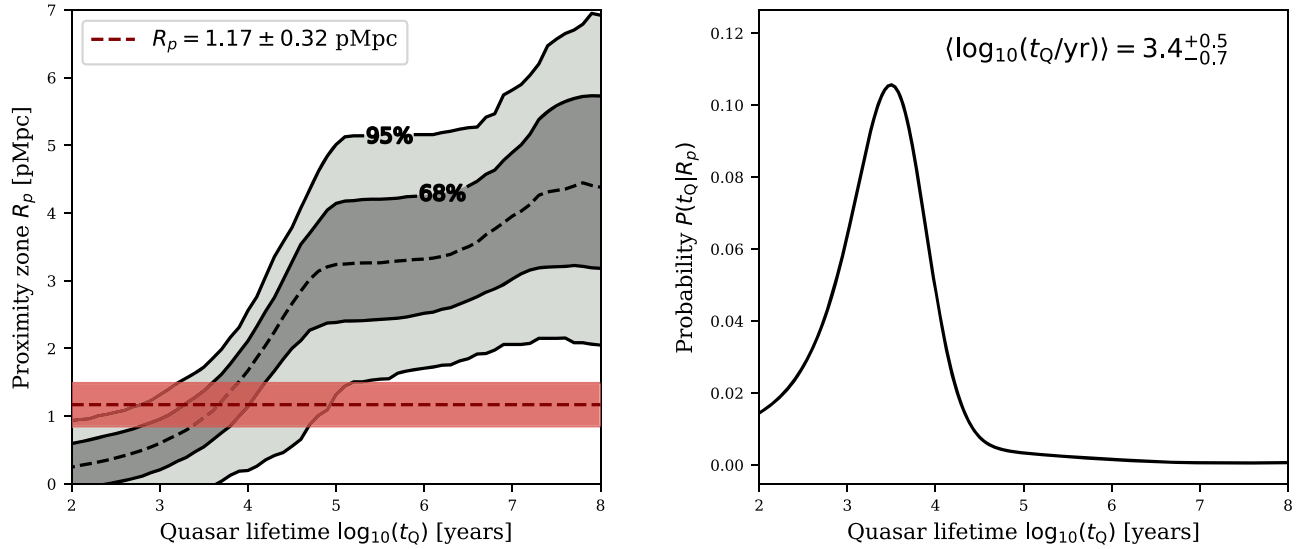

Figure 8. Left panel: dependence of proximity zone size R_p on quasar lifetime (t_Q), adopted from literature (Davies et al. 2016; Eilers et al. 2017) who have done radiative transfer simulations for quasars with similar absolute magnitude ($M_{1450} = 26.67$) and redshift ($z = 6.3401$) as PSO J083+11. $R_p = 1.17 \pm 0.32$ is indicated by red lines. Right panel: probability distribution of t_Q which shows that PSO J083+11 is a young object with $t_Q = 10^{3.4\,\pm\,0.7}$ yr (95% confidence interval).

and a redshift of 6.3401 ± 0.0004. With respect to [C II] (host galaxy tracer), the Mg II (quasar BLR tracer) is redshifted by 237 ± 150 km s^{-1}. As a comparison, Schindler et al. (in preparation) found that Mg II in high-z quasars can be significantly shifted with respect to the [C II] with a median velocity shift of -416^{+304}_{-398} km s^{-1}. The Mg II line, which arises from the BLR, may experience strong internal motions or winds, potentially displacing the emission line centers from the systemic redshift (Mazzucchelli et al. 2017).

7.3. Moment Maps for [C II] and Dust Continuum Emission

We covered two dust continuum spectral windows in our observation, one centered at 244 GHz and the other at 258 GHz. Pure continuum data are produced by selecting channels that are free from line emission, where we chose the effective bandwidth for each spectral window to be around 2500 km s^{-1}. Then, we collapsed each spectral window to create a moment-zero map of the dust continuum. The final 244 GHz and 258 GHz dust continuum maps have rms noise levels of 30.7 and 35.8 μJy beam^{-1}, respectively. Figure 10 shows the continuum map centered at 258 GHz. By using the same circular aperture size as for [C II]—i.e., a radius of 1.″5—we obtain flux densities of $S_{244\,\mathrm{GHz}} = 5.10 \pm 0.15$ mJy and $S_{258\,\mathrm{GHz}} = 5.54 \pm 0.16$ mJy. The moment-zero map of [C II] is also created by collapsing the 700 km s^{-1} cube width as shown in Figure 10. This width is equivalent to 3 × [C II] FWHM.

As is visible in Figure 10, both continuum and [C II] emission are spatially resolved with approximate sizes of 2.3 kpc × 1.7 kpc and 8.2 kpc × 4.3 kpc, respectively. These sizes are defined as the major and minor axis FWHMs of the 2D Gaussian function, which is fitted to those emissions. In addition, the continuum emission peak overlaps with the central [C II] emission. In Figure 11, we show the velocity field and dispersion maps of the continuum-subtracted [C II] emission.[23] A mild velocity gradient is seen with the northern part redshifted and the southern part blueshifted. The

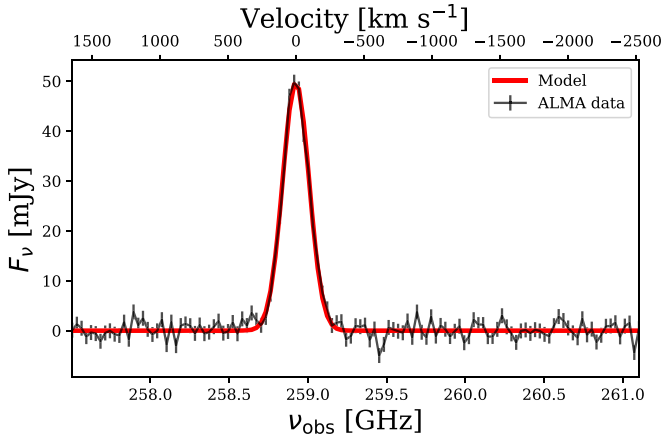

Figure 9. PSO J083+11 continuum-subtracted [C II] spectrum, extracted with a 1.″5 aperture radius. The data (black) are fitted to a Gaussian function (red). The upper axis shows velocities centered at $z = 6.3401$.

morphology in Figure 10 is seen as a single resolved blob while the integrated spectrum (Figure 9) is represented well by a simple Gaussian profile.

Finally, we overlaid the ALMA moment maps on the PSF-subtracted HST image as seen in Figure 12. Previously, we identified a potential lensing galaxy as shown in Figure 4. However, there is no apparent dust or [C II] emission at the position of this potential lensing companion (see Figure 12), which makes it unlikely to be physically associated.

7.4. Star Formation Rate

To derive a star formation rate in the quasar host galaxy, we first calculate the [C II] 158 μm line luminosity following Carilli & Walter (2013):

$$\frac{L_{\mathrm{line}}}{L_\odot} = 1.04 \times 10^{-3} \frac{S_{\mathrm{line}}\Delta v}{\mathrm{Jy\ km\ s^{-1}}} \left(\frac{D_L}{\mathrm{Mpc}}\right)^2 \frac{\nu_{\mathrm{obs}}}{\mathrm{GHz}}. \quad (15)$$

We obtain a luminosity of $L_{[\mathrm{C\,II}]} = (1.04 \pm 0.04) \times 10^{10}\,L_\odot$, which interestingly makes this one of the most luminous [C II]

[23] See the moment map equations and sigma line-width map definition in https://spectral-cube.readthedocs.io/en/latest/moments.html.

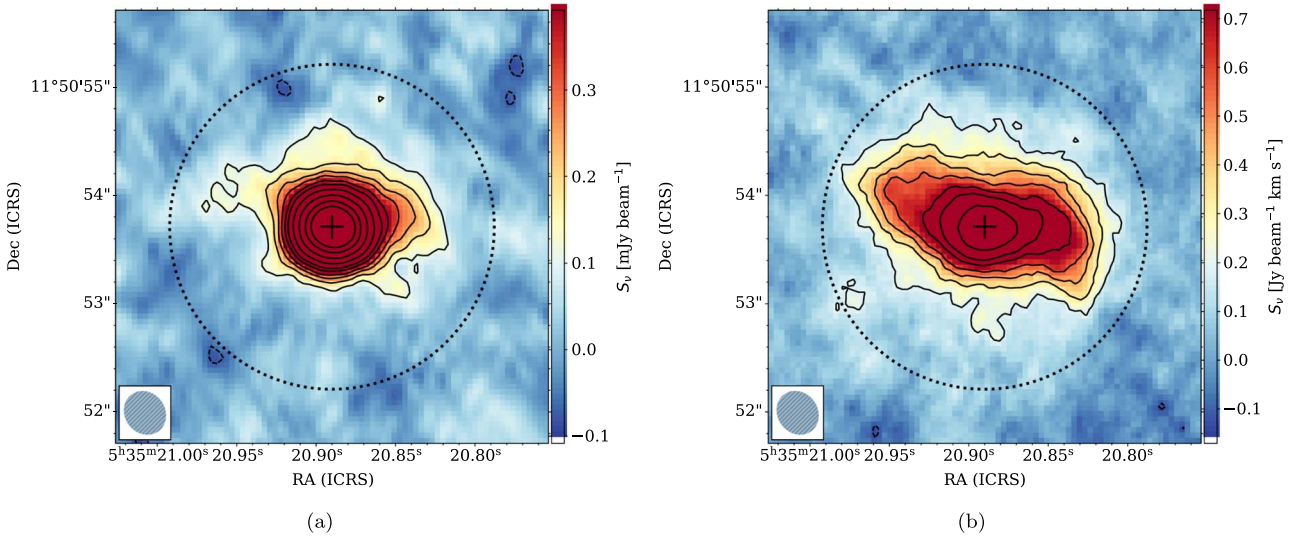

Figure 10. The PSO J083+11's ALMA dust continuum (left) and [C II] velocity-integrated (right) maps. The size of the synthesized beam can be seen at the bottom left of each panel. The solid lines in the left panel represent the [3, 5, 7, 9, 12, 15, 21, 30, 42, 54] × σ contours with $\sigma = 0.04$ mJy beam^{-1} for the continuum flux density while the right panel shows $\sigma = 0.06$ Jy beam^{-1} km s^{-1} for the [C II] velocity-integrated flux. Negative contours are shown as dashed lines. The 1.″5 (8.3 kpc) aperture size that was applied to calculate the total flux density is represented by the dotted circles. The position of the quasar is marked with a black cross.

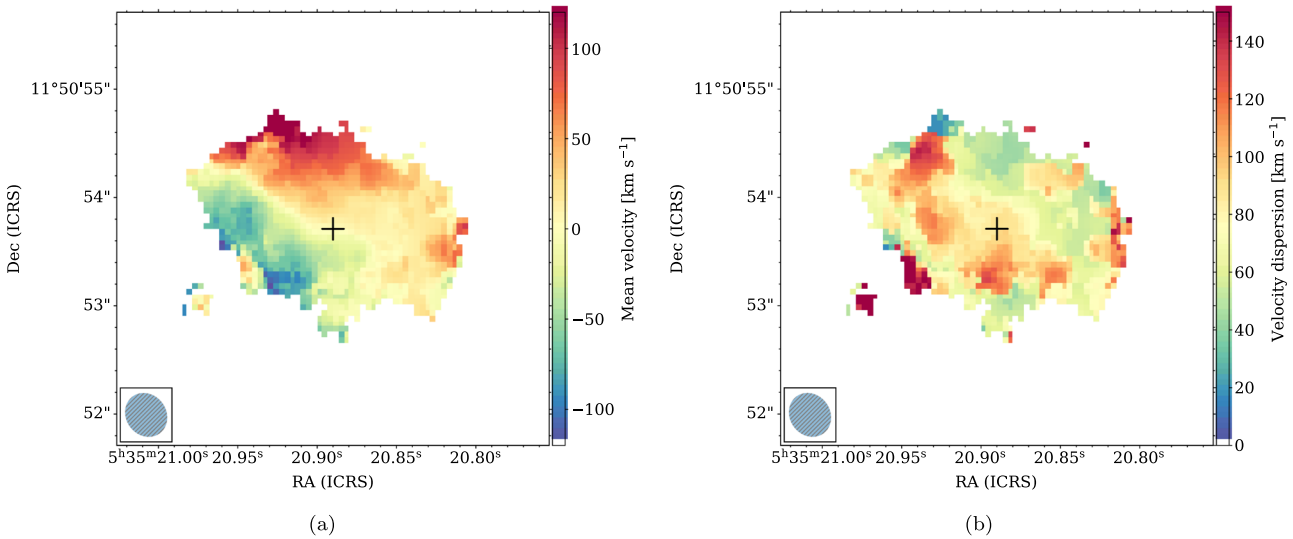

Figure 11. Maps of [C II] intensity-weighted velocity (mean velocity field, left panel) and intensity-weighted velocity dispersion (right panel) for PSO J083+11. Note that we exclude those pixels with $<3\sigma$ detection in the integrated [C II] flux (see Figure 10). The beam size is shown in the bottom left. The position of the quasar is marked with a black cross.

line $z > 6$ quasars detected to date (Decarli et al. 2018; Venemans et al. 2018). The star formation rate (SFR) can be estimated by applying the De Looze et al. (2014) SFR–$L_{[\mathrm{C\,II}]}$ scaling relations for $z > 5$ galaxies:

$$\frac{\mathrm{SFR}_{[\mathrm{C\,II}]}}{M_\odot \mathrm{yr}^{-1}} = 3.0 \times 10^{-9} \left(\frac{L_{[\mathrm{C\,II}]}}{L_\odot} \right)^{1.18}. \quad (16)$$

This will give us a value of the $\mathrm{SFR}_{[\mathrm{C\,II}]} \sim 1990\, M_\odot\ \mathrm{yr}^{-1}$. However, one needs to take into account a factor of ∼2.5 for the systematic uncertainty from the scaling relation which makes the possible range of derived SFR for PSO J083 +11 $\mathrm{SFR}_{[\mathrm{C\,II}]} = 800 - 4900\, M_\odot\ \mathrm{yr}^{-1}$.

Another important parameter that we can estimate from the ALMA data are the total infrared luminosity (L_{TIR}, rest-frame 3–1100 μm), far-infrared luminosity (L_{FIR}, rest-frame 42.5–122.5 μm), and the dust mass, from which we can again calculate an independent star formation rate (e.g., Helou et al. 1988; Kennicutt & Evans 2012; Carilli & Walter 2013). This can be done by assuming low dust optical depth in the Rayleigh–Jeans regime, thus modeling the SED with a modified blackbody will be sufficient (e.g., Beelen et al. 2006; Novak et al. 2019). The expression is

$$S_{\nu_{\mathrm{obs}}} = f_{\mathrm{CMB}} (1+z) (D_L)^{-2} \kappa_{\nu_{\mathrm{rest}}} M_{\mathrm{dust}} B_{\nu_{\mathrm{rest}}} (T_{\mathrm{dust},z}), \quad (17)$$

where $B_{\nu_{\mathrm{rest}}}$ is the blackbody radiation function, D_L is the luminosity distance, M_{dust} is the dust mass, while the observed and rest frequencies are related as $\nu_{\mathrm{rest}} = (1+z)\nu_{\mathrm{obs}}$, and all values are in SI units. The adopted opacity coefficient following

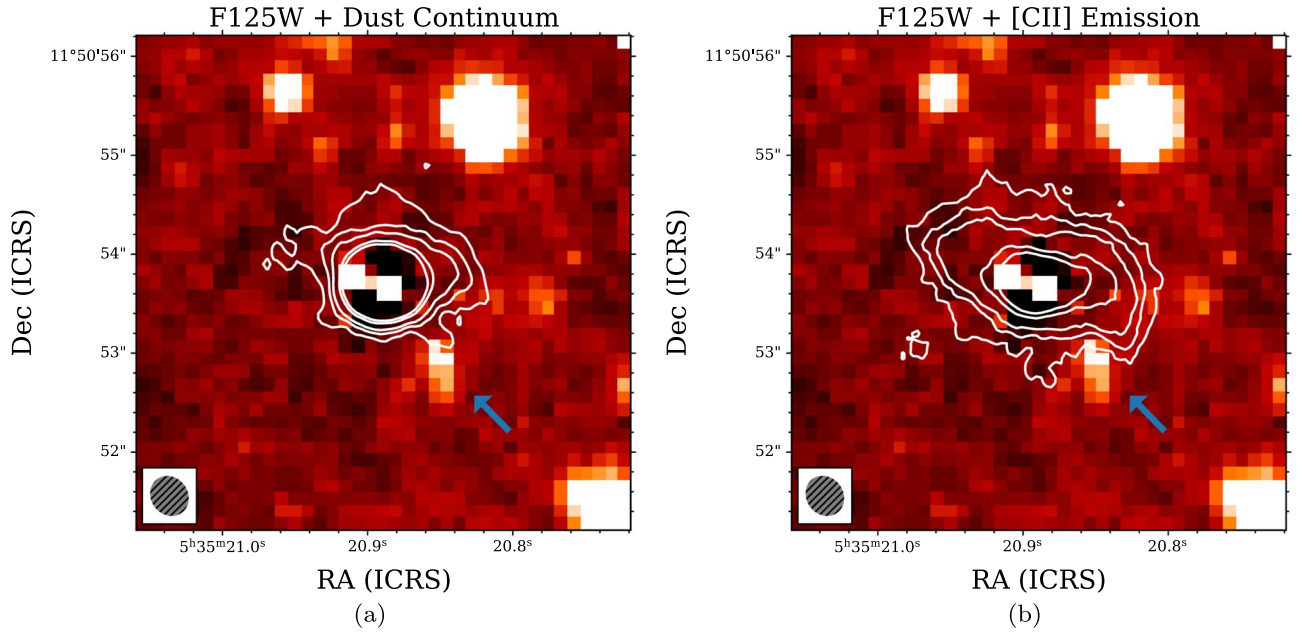

Figure 12. PSF-subtracted HST image of PSO J083+11 with an overlay of ALMA dust continuum and [C II] emission maps as contours (from Figure 10). The white solid lines in the left panel represent the [3, 5, 7, 12, 15] × σ contours with $\sigma = 0.04$ mJy beam^{-1} for the continuum while the right panel shows $\sigma =$ 0.06 Jy beam^{-1} km s^{-1} for the [C II] emission maps. Unlike Figure 4, this PSF-subtracted HST image has been rotated so north is up and east is left. The beam size for ALMA data is shown in the bottom left. The neighboring potential foreground galaxy is located to the southwest from the central quasar (blue arrow). There is no apparent dust or [C II] emission at the location of this neighbor, which makes it unlikely to be a physical companion.

Dunne et al. (2003) and Novak et al. (2019) is

$$\kappa_{\nu_{\rm rest}} = \kappa_{\nu_0}\left(\frac{\nu_{\rm rest}}{\nu_0}\right)^{\beta} = 2.64\left(\frac{\nu_{\rm rest}}{c/125\ \mu{\rm m}}\right)^{\beta}\ {\rm m^2\ kg^{-1}}, \quad (18)$$

where c is the speed of light and β is the dust spectral emissivity index. Note that the estimated dust mass will have at least a factor of 2 for the systematic uncertainty due to the adopted opacity coefficient scaling relation.

Dust heating by the cosmic microwave background (CMB) plays an important role at $z \gtrsim 6$ and needs to be taken into consideration following da Cunha et al. (2013), namely,

$$f_{\rm CMB} = 1 - \frac{B_{\nu_{\rm rest}}(T_{{\rm CMB},z})}{B_{\nu_{\rm rest}}(T_{{\rm dust},z})}, \quad (19)$$

$$T_{{\rm dust},z} = (T_{\rm dust}^{\beta+4} + T_{{\rm CMB},z=0}^{\beta+4}[(1+z)^{\beta+4} - 1])^{\frac{1}{\beta+4}}, \quad (20)$$

where $T_{\rm dust}$ is the intrinsic dust temperature of the source assuming it is located at redshift zero and $T_{\rm CMB} = 2.73(1+z)$ K is the temperature of the CMB at a given z. In our case, $T_{\rm CMB} = 20.04$ K.

Note that we only have two data points of the continuum measurements—at 244 and 258 GHz—both of them located on the Rayleigh–Jeans tail and not reaching the dust SED peak. This prohibits us from constraining the full SED shape and dust temperature due to degenerate fitting parameters. Hence, further assume that $T_{\rm dust} = 47$ K and $\beta = 1.6$, which are usually applied for quasar host galaxies at $z \gtrsim 6$ (e.g., Beelen et al. 2006; Decarli et al. 2018; Venemans et al. 2018). Scaling the SED model (Equation (17)) to the observed FIR photometry at 244 and 258 GHz results in $M_{\rm dust} = (4.88 \pm 0.14) \times 10^8\ M_\odot$. By integrating the SED, we obtain $L_{\rm FIR} = (1.22 \pm 0.07) \times 10^{13}\ L_\odot$ and $L_{\rm TIR} = (1.72 \pm 0.09) \times 10^{13}\ L_\odot$. This high luminosity means that PSO J083+11 can be classified as a hyperluminous infrared galaxy (HyLIRG, $L_{\rm TIR} > 10^{13}\ L_\odot$).

The TIR luminosity can be converted to an SFR by utilizing the relation from Murphy et al. (2011) and Kennicutt & Evans (2012):

$${\rm SFR_{TIR}}[M_\odot\ {\rm yr^{-1}}] = 1.49 \times 10^{-10} L_{\rm TIR}[L_\odot]. \quad (21)$$

This gives us ${\rm SFR_{TIR}} \sim 2560\ M_\odot\ {\rm yr^{-1}}$. Accounting for the factor of 3 of systematic uncertainty in the scaling relation, we obtain the 1σ possible range of ${\rm SFR_{TIR}} = 900$–$7600\ M_\odot\ {\rm yr^{-1}}$. This is consistent with SFR estimates based on the [C II] luminosity above. A summary of the calculated parameters is shown in Table 2.

To compare the PSO J083+11 host galaxy properties with other $z \gtrsim 6$ quasars, we took $L_{\rm [C\,II]}$ and $L_{\rm FIR}$ measurements from the literature (Walter et al. 2009; Venemans et al. 2012; Wang et al. 2013, 2016; Willott et al. 2013, 2015, 2017; Bañados et al. 2015; Venemans et al. 2016; Mazzucchelli et al. 2017; Decarli et al. 2018), which were recalculated by Decarli et al. (2018). We also added 10 young quasars studied by Eilers et al. (2020). As seen in Figure 13, PSO J083+11 shows values of $L_{\rm [C\,II]}$ and $L_{\rm FIR}$ comparable to those high-z quasars with the highest SFR and FIR emission.

8. Discussion: a Young Weak-line Quasar?

Type 1 active galactic nuclei (AGNs) intrinsically exhibit strong broad-line emission in the optical and ultraviolet rest-frame regime. However, this is not the case for WLQs, which show unusually weak or no emission line. It is well established that WLQs are not BL Lacertae objects, which usually have spectra dominated by a relatively featureless nonthermal emission continuum due to the effects of the relativistic jet closely aligned to the line of sight of the observer (Diamond-Stanic et al. 2009). Also, the majority of WLQs are radio quiet, and they are not related to broad absorption-line phenomenon (e.g., Kumar et al. 2018).

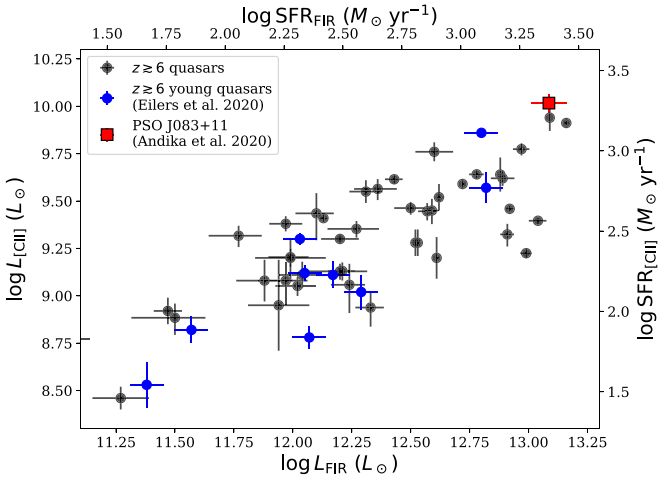

Figure 13. The comparison between the star formation rate estimated from the dust continuum luminosity (following Murphy et al. 2011 and Kennicutt & Evans 2012) and the [C II] luminosity (following De Looze et al. 2014) using the assumption of $T_{dust} = 47$ K. A sample of $z \gtrsim 6$ quasars from the literature (black dots; see text) and $z \gtrsim 6$ young quasars (blue dots, Eilers et al. 2020) are shown. PSO J083+11 (red square) shows values of $L_{[C\,II]}$ and L_{FIR} comparable to those high-z quasars with the highest SFR and FIR emission. For clarity, the error bars of PSO J083+11 have been multiplied by three.

Diamond-Stanic et al. (2009) and Shemmer et al. (2006) established that WLQs are a rare, unique population as their nature could not be explained by gravitational macro- or microlensing. In the case of PSO J083+11, our HST observations revealed a potential lensing galaxy located at $\theta \sim 1''$ from the central quasar. However, the maximum magnification of $\mu \leqslant 1.07$ does not provide significant boosting to the apparent quasar continuum emission. In addition, we showed that PSO J083+11's UV-to-optical (Figure 1) and far-infrared SED (Section 7.4) is similar to those of ordinary quasars, not a strongly lensed galaxy. Based on these measurements, the weak-line nature of PSO J083+11 cannot be explained by strong gravitational macrolensing. Note that to completely rule out microlensing, we would need spectroscopic monitoring and to search for the reappearance of emission lines. For a stellar lens in a foreground galaxy, the characteristic timescale for microlensing is ~10 yr (Gould 1995). Nevertheless, the closest foreground galaxy that we found in the HST image is already far enough from the central quasar ($\theta > \theta_E$; see Section 5.2), making a microlensing interpretation unlikely.

Several theories have been proposed to explain the WLQ phenomenon. and according to Plotkin et al. (2015), they can be classified into two broad categories: (1) soft ionizing continuum theory and (2) anemic broad emission line region model. In this section, we will discuss the most probable explanation for the observed weak-line nature of PSO J083+11.

8.1. Soft Continuum Due to Super-Eddington Accretion?

One might expect that the BLR is less photoionized so the broad emission lines produced are weak due to soft ionizing continuum. How could this happen? The first proposed mechanism is an intrinsically soft continuum due to a cold accretion disk around a slowly accreting, very massive black hole (Laor & Davis 2011; Plotkin et al. 2015), although this possibility is rather low in the case of PSO J083+11. This is because the required critical mass is $M_{BH} > 3.6 \times 10^9\,M_\odot$ for a nonrotating ($a = 0$) or $M_{BH} > 1.4 \times 10^{10}\,M_\odot$ for a nearly maximally rotating ($a = 0.998$) black hole, while the mass estimated for PSO J083+11 is already a factor of ~2 smaller than the lower of these limits (see Section 4.4). In addition, according to Volonteri et al. (2013), high-z SMBHs should be rapidly spinning, which would yet increase this difference.

The second proposed mechanism is a quasar with a high Eddington ratio that is expected to have an optically and geometrically thick inner accretion disk, a so-called slim disk (Luo et al. 2015). The scale height of this thick disk grows as a function of Eddington ratio and becomes a shielding component, which prevents the high-energy photons from the central region to reach and ionize the BLR, leading to the observed weak, high-ionization line emission (Ni et al. 2018). This model has been corroborated by observation of WLQs with weak X-ray emission that typically show harder X-ray spectra compared to normal quasars, indicating intrinsic X-ray absorption in these objects (Wu et al. 2011, 2012). However, we cannot completely rule out the possibility of the presence of shielding gas between the accretion disk and BLR due to the lack of X-ray spectroscopy for PSO J083+11.

The third proposed mechanism is that an extremely high accretion rate could lead to less efficient production of X-rays, which results in an SED that peaks in the ultraviolet (Leighly et al. 2007a, 2007b). This could be related to a quenched X-ray corona, making it smaller in size, or alternatively, X-ray photons that are trapped and advected into the black hole before they can diffuse out. In other words, in these scenarios, there would not be enough high-energy photons emitted from the continuum source to produce high-ionization potential lines like C IV. However, there would be no problems with producing lower-ionization lines (e.g., Hα, Hβ, and Mg II).

The second and third aforementioned mechanisms suggest that on average the low-z WLQs have significantly higher Eddington ratios and luminosities compared to other normal low-z quasars (Meusinger & Balafkan 2014). In contrast, we do not see this behavior for PSO J083+11 compared to other high-z quasars because its Eddington ratio is based on the Mg II line, and the underlying continuum is not particularly strong ($L_{bol}/L_{Edd} \sim 0.5$; see Figure 3). However, we have to note that the virial-mass calculation relies on the empirical scaling relation derived via reverberation mapping, which might be inadequate in the case of WLQs due to the weakness of their emission lines (Luo et al. 2015). The calculated black hole mass tends to be underestimated, making the actual Eddington ratio potentially lower than currently estimated (Marculewicz & Nikolajuk 2019). Moreover, the typical systematic error of the single-epoch virial-mass approach is ≈0.4–0.5 dex (Shen 2013) and could be larger if the Mg II BLR is complex and may not be virialized yet in these kinds of exceptional objects (Plotkin et al. 2015).

Another potential indicator of extremely high accretion rate is the shape of the continuum itself, as found in a super-Eddington ($L_{bol}/L_{Edd} \geqslant 9$) quasar, PSO J006+39, at $z \sim 6.6$ with a very blue continuum that was studied by Tang et al. (2019). This Eddington ratio was estimated by modeling the SED of the UV continuum, where they obtained a power-law slope index, $\alpha_\lambda = -2.94 \pm 0.03$. This is significantly bluer than the slope of $\alpha_\lambda = -2.33$ predicted from the standard thin disk model (Shakura & Sunyaev 1973). Although PSO J006+39 is accreting at a super-Eddington rate, it is not a WLQ (EW (C IV)$_{rest} \sim 84$ Å). Compared to that object, our measured power-law slope index is consistent with a typical quasar

($\alpha_\lambda = -1.66 \pm 0.01$) and not steeper than those aforementioned models, indicating the absence of super-Eddington accretion. Hence, overall, soft continuum models seem inadequate to explain the weak-line nature of PSO J083+11.

8.2. Are WLQs Young Quasars?

With the caveats of all the scenarios presented in Section 8.1, trying to explain the WLQ nature, another potential explanation for the weak-line nature might lie in gas-deficient or anemic BLR clouds, due to the quasar being in the beginning of its accretion phase. In the first scenario, there might be only a small amount of gas and/or covering factor in the BLR of WLQs (Shemmer et al. 2010; Nikołajuk & Walter 2012). If this is true, all broad lines should have small flux and equivalent widths. However, unlike normal quasars, WLQs have relatively small EW $(\mathrm{C\,IV})_{\mathrm{rest}}$/EW $(\mathrm{H}\beta)_{\mathrm{rest}}$ line ratios, which are inconsistent with their BLRs simply having low gas content or small covering factors, although it could play a secondary role (Plotkin et al. 2015).

On the other hand, the second scenario proposed that in the beginning of an AGN phase, BLRs are still bare because the material from the accretion disk has not yet have sufficient time to reach the region where broad lines will later form (Hryniewicz et al. 2010). With the assumption that the wind from the disk has velocities of $\approx$100 km s^{-1}, the time needed to form the BLR is around $\sim 10^3$ yr (Hryniewicz et al. 2010). Therefore, if WLQs are indeed an evolutionary quasar phase, they should be rare. An interesting discovery is that the fraction of WLQs among quasars seems to increase with redshift (e.g., Diamond-Stanic et al. 2009; Bañados et al. 2016; Shen et al. 2019). In this picture of a still-forming BLR during the WLQ phase, higher-ionization species such as C IV would be the weakest because they originate in a region higher above the disk that is not fully formed yet. On the other hand, low-ionization species (e.g., Hβ, Mg II) that are formed close to the accretion disk may look normal (Plotkin et al. 2015).

We should emphasize that most low-z WLQ studies do not have access to Lyα and the quasar lifetime could not be determined with the method that we explained in Section 6. At $z > 6$, the proximity zones are sensitive to the lifetime of the quasars as the intergalactic gas has a finite response time to the quasars' radiation. The accretion lifetime of PSO J083+11 as derived from its proximity zone gives us a range of $t_{\mathrm{Q}} = 10^{3.4\pm0.7}$ yr, consistent with the BLR formation time at the lower end. Hence, there is a possibility that the BLR in this object is not fully formed yet, leading to the observed weak emission line signature in the spectrum (Hryniewicz et al. 2010). However, as pointed out by Eilers et al. (2018), this quasar could have a higher actual age of substantial accretion compared to the one estimated from its proximity zone size. In that case, it could have been growing in a highly obscured phase and the UV continuum radiation had only broken out of this obscuring medium $\sim 10^3$ to 10^4 yr before (see also Hopkins et al. 2005; DiPompeo et al. 2017; Mitra et al. 2018). This might be caused by a huge dust and gas supply at high redshifts, funneled into the center of the host galaxy feeding both star formation and SMBH, but hiding the quasar within it. In line with that, even though tailored at lower-z systems, Sanders et al. (1988a) argued that ultraluminous infrared galaxies (ULIRGs) could be the initial stage of a quasar when heavy obscuration was present. Only at the end of this incipient dust-enshrouded phase would the quasar be revealed in the optical as an unobscured source (e.g., Sanders et al. 1988b; Sanders & Mirabel 1996; Hopkins et al. 2008). A model proposed by Liu & Zhang (2011) even predicts that the quasars that have just become unobscured should exhibit no broad emission lines because the BLR would form at a later stage when the dusty torus supplies the fuel to the accretion disk. The luminous FIR properties that we found in Section 7.4 would suggest that PSO J083+11 is just at the beginning of its unobscured quasar phase while the host galaxy still experiences highly active star formation. This picture is well consistent with the young accretion lifetime derived from the proximity zone size measurement.

8.3. A Small Caveat Regarding the Small Proximity Zone Size

Above, we attributed the small proximity zone of PSO J083+11 to a limited unobscured accretion lifetime. There is a hypothetical alternative, the truncation of PSO J083+11's proximity zone due to the presence of an absorption system within $\leqslant$10,000 km s^{-1} (or $z > 6.3$) in front of the quasar, just around the edge of the proximity zone. Such a system, like a damped Lyα system (DLA) or Lyman limit system (LLS), would block ionizing radiation from the quasar to the IGM due to its optically thick nature at the Lyman limit (Eilers et al. 2017, 2018; D'Odorico et al. 2018; Bañados et al. 2019; Farina et al. 2019).

In Figure 14, we show hypothetical absorption systems at $z = 6.295$ (or $z = 2.233$, see below) that might be able to truncate the proximity zone. This redshift value is equivalent to a distance of $R \approx 2.43$ pMpc from the central quasar. For comparison, the proximity zone size that we obtained in Section 6 is $R_p = 1.17 \pm 0.32$ pMpc. The redshift of that system was chosen so that the associated N V $\lambda\lambda$1238, 1242 match the position of the two strong absorption lines observed at 9037 Å and 9066 Å. However, the positions of other lines that should be present in DLAs (e.g., Si II λ1260, O I λ1302, Si IV λ1402, etc.) do not match any potential absorption lines seen in the observed spectrum. The presence of low-ionization lines is particularly important because they usually indicate an optically thick self-shielding absorption system (Eilers et al. 2020), which can truncate the proximity zone. Also, by considering that the inferred distance between the absorber and quasar is not really close, the proximity zone might be influenced by such a hypothetical absorber, but would unlikely be significant.

In contrast, there is also an alternative possibility that the two strong absorption lines mentioned before are associated with Mg II $\lambda\lambda$2796,2803 from a lower-redshift ($z = 2.233$) absorption system instead. However, we have to note that searching for very weak metal absorption features with our current spectrum is difficult due to the low resolution. A more thorough analysis to put stringent constraints on potentially associated absorption systems will be done with VLT/MUSE data, and we report on this in our next paper (I. T. Andika et al. 2020, in preparation).

9. Summary and Conclusion

In this paper, we presented our effort to increase the number of known quasars at $z > 6$, which led to the discovery of PSO J083+11, a new WLQ at $z = 6.3401$. This object was identified using imaging data from PS1, UHS, and unWISE. This discovery shows that our SED-fitting-based quasar selection to

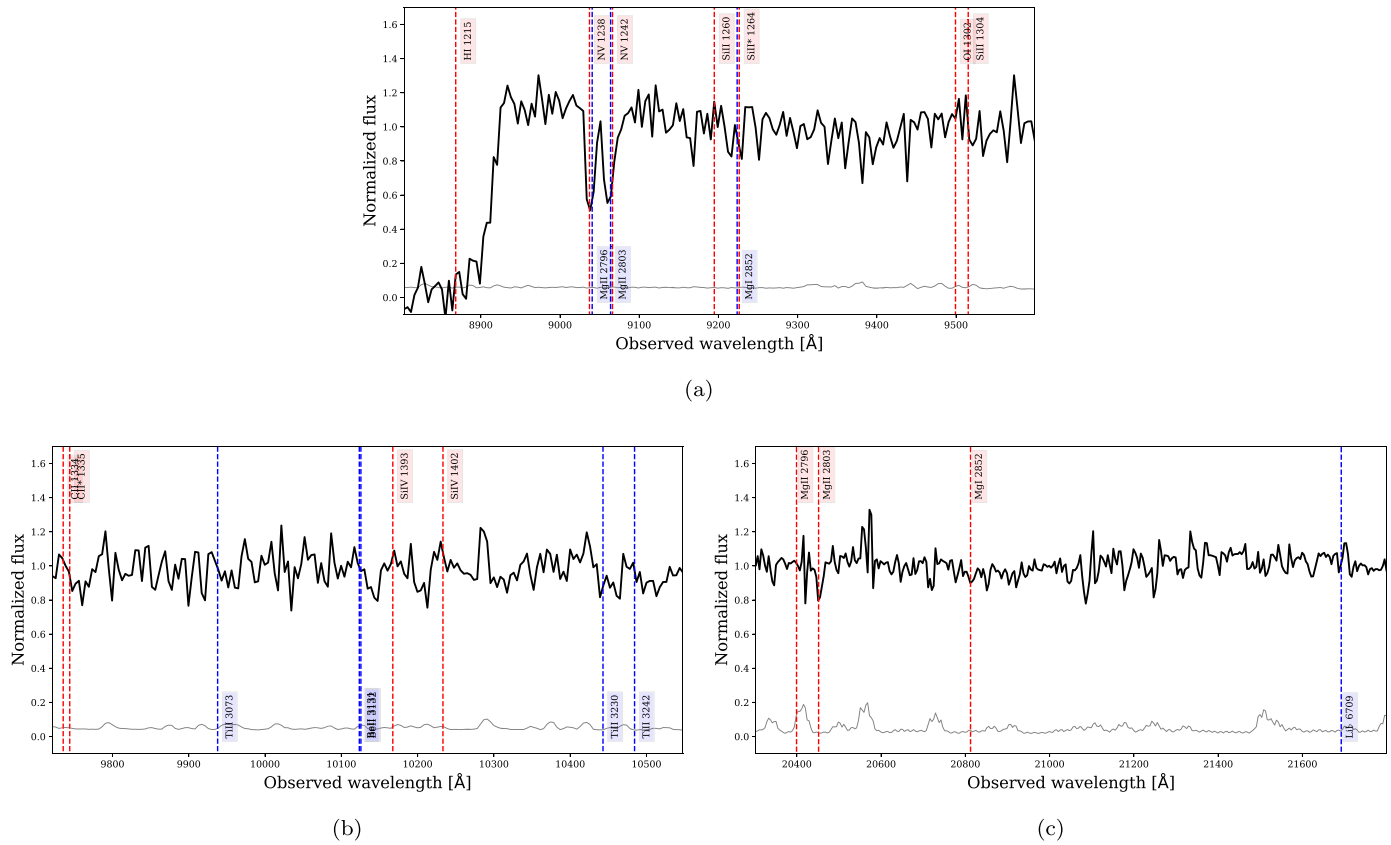

Figure 14. The GNIRS spectrum of PSO J083+11, normalized to the continuum (black). The positions of the expected metal lines coming from the hypothetical absorption system in front of the quasar at $z = 6.295$ and $z = 2.233$ are shown in red and blue, respectively. The gray line indicates the noise spectrum. No strong metal lines are found at the expected positions (albeit with low spectral resolution data), making the presence of a DLA or LLS very close to the quasar unlikely.

identify quasar candidates from large sky imaging surveys is successfully finding quasars and can be adapted and extended to find larger samples at the highest redshifts.

Our main results on PSO J083+11 can be summarized as follows:

1. By using the NIR spectra from Gemini/GNIRS, we modeled the Mg II emission and the underlying continuum to derive a black hole mass of $\log(M_{\rm BH}) = 9.30^{+0.16}_{-0.10}\ M_\odot$ and Eddington ratio of $L_{\rm bol}/L_{\rm Edd} = 0.51^{+0.13}_{-0.17}$. This confirms that this object is powered by an actively accreting SMBH with an accretion rate similar to those of the most luminous low- and high-z quasar populations.
2. Lyα+N V emission in this quasar is weak (EW (Lyα + N V)$_{\rm rest} = 5.65^{+0.72}_{-0.66}$ Å), suggesting that this is a weak-line quasar. The weak-line nature of Lyα+N V is not likely caused by IGM strong absorption in the line of sight. This is supported by the absence of C IV emission (EW (C IV)$_{\rm rest} \leqslant 5.83$ Å), which suggests that the strength of the BLR emission is intrinsically weak. The spectrum shows a very small proximity zone $R_{\rm p} = 1.17 \pm 0.32$ pMpc, which suggests a current quasar lifetime of only $10^3 - 10^{4.5}$ yr, at odds with the SMBH mass having formed with the observed instantaneous accretion rate.
3. From HST/WFC3 imaging in the F125W filter, we found a potential intervening galaxy located 1″ to the southwest direction from the central quasar with a magnitude = 25.42 ± 0.07. Assuming that it is a star-forming main-sequence galaxy at lower redshift and using a point-mass gravitational lens configuration, we find an upper limit of possible lensing magnification $\mu \leqslant 1.07$, implying no relevant effect of boosting to quasar apparent emission. The quasar is also observed as a pure point source with no additional emission component.
4. ALMA band-6 observations for PSO J083+11 have detected both dust continuum and spatially resolved [C II] emission from the host galaxy. We derived an accurate redshift from [C II] ($z_{\rm [C\,II]} = 6.3401 \pm 0.0004$). The resolved extended morphology of this line might be caused by a remnant of a merger or in any case unrelaxed ongoing formation. This quasar is among the most luminous [C II] emitters to date. Modeling the Rayleigh–Jeans tail of dust continuum with a modified blackbody function gives us a constraint on the dust mass of $M_{\rm dust} = (4.88 \pm 0.14) \times 10^8\ M_\odot$ and star formation rate of ${\rm SFR_{TIR}} = 900 - 7600\ M_\odot\ {\rm yr}^{-1}$, similar to that of HyLIRGs. This value is also consistent with the SFR derived from the [C II] emission (${\rm SFR_{[C\,II]}} = 800 - 4900\ M_\odot\ {\rm yr}^{-1}$).
5. Considering the quasar lifetime of PSO J083+11 and BLR formation timescale, we propose that the weak emission line profile in our young quasar spectrum is caused by a BLR that is not fully formed yet rather than continuum boosting by gravitational lensing or soft continuum emission due to super-Eddington accretion. However, we cannot completely rule out the possibility of the presence of shielding gas between the accretion disk and BLR due to the lack of X-ray spectroscopy.

Overall, this quasar paints a puzzling picture of an SMBH, at odds with seemingly only a very recent onset of currently

moderate accretion. In the future, a thorough search for potentially associated absorption systems which could affect the accuracy of our quasar lifetime estimation will be done with VLT/MUSE data. The availability of X-ray spectra from facilities like XMM-Newton or Chandra would be very beneficial to get better constraints on the SED modeling and accretion rate, and to check the possibility of shielding gas possibly present between the accretion disk and BLR.

In the context of an early phase of quasar (re)activation, the narrow emission line region will take a longer time to form compared to the broad emission line region and is likely to be absent in this particular stage (Hryniewicz et al. 2010). Future facilities like the James Webb Space Telescope (JWST) will enable us to observe $z > 6$ WLQs in the mid-infrared. Hence, we can test for this hypothesis by constraining the NLR properties and tracing the presence of this region by studying the [O III] λ5007 line profile. Further statistical studies, supported by a larger sample of WLQs at the highest accessible redshifts, are required to establish connections between normal quasars, young quasars, and those that are weak-lines. This will play an important role in our understanding of quasar evolution, the rapid formation of the first SMBHs, and structure formation in general in the universe at the dawn of cosmic time.

We thank the anonymous referees for constructive comments on the manuscript. We would like to thank Dian P. Triani for the fruitful discussions on modeling the star-forming main-sequence galaxy and Anton T. Jaelani for the valuable insight regarding the gravitational lensing model. We gratefully acknowledge the assistance of Joseph F. Hennawi and Iskren Georgiev on reducing the spectra and correcting the telluric absorption. We also would like to thank Frederick Davies for providing his radiative transfer code to estimate the quasar's lifetime. I.T.A. is extremely grateful to Adriana Larasati and Fenyka A. Jeanuarieke, who give unending encouragement and for always being there, especially in the most difficult moments.

F.W., B.P.V., Ml.N., and M.N. acknowledge the support from ERC Advanced grant 740246 (Cosmic Gas). A.-C.E. acknowledges support by NASA through NASA Hubble Fellowship grant #HF2-51434 awarded by the Space Telescope Science Institute, which is operated by the Association of Universities for Research in Astronomy, Inc., for NASA, under contract NAS5-26555. I.T.A. acknowledges support from the International Max Planck Research School for Astronomy and Cosmic Physics at the University of Heidelberg (IMPRS-HD). This work was supported by the Deutsches Zentrum für Luft- und Raumfahrt (DLR) under grant number 50 OR 2001.

The Pan-STARRS1 Surveys (PS1) and the PS1 public science archive have been made possible through contributions by the Institute for Astronomy, the University of Hawaii, the Pan-STARRS Project Office, the Max-Planck Society and its participating institutes, the Max Planck Institute for Astronomy, Heidelberg, and the Max Planck Institute for Extraterrestrial Physics, Garching, The Johns Hopkins University, Durham University, the University of Edinburgh, the Queen's University Belfast, the Harvard-Smithsonian Center for Astrophysics, the Las Cumbres Observatory Global Telescope Network Incorporated, the National Central University of Taiwan, the Space Telescope Science Institute, the National Aeronautics and Space Administration under grant No. NNX08AR22G issued through the Planetary Science Division of the NASA Science Mission Directorate, the National Science Foundation grant No. AST-1238877, the University of Maryland, Eötvös Loránd University (ELTE), the Los Alamos National Laboratory, and the Gordon and Betty Moore Foundation.

This paper makes use of the following ALMA data: ADS/JAO.ALMA#2019.1.01436.S. ALMA is a partnership of ESO (representing its member states), NSF (USA), and NINS (Japan), together with NRC (Canada), MOST and ASIAA (Taiwan), and KASI (Republic of Korea), in cooperation with the Republic of Chile. The Joint ALMA Observatory is operated by ESO, AUI/NRAO and NAOJ.

Part of data presented in this paper is based on observations obtained at the international Gemini Observatory (GN-2019A-FT-204). The Gemini Observatory is managed by the Association of Universities for Research in Astronomy (AURA) under a cooperative agreement with the National Science Foundation. On behalf of the Gemini Observatory partnership: the National Science Foundation (United States), National Research Council (Canada), Agencia Nacional de Investigación y Desarrollo (Chile), Ministerio de Ciencia, Tecnología e Innovación (Argentina), Ministério da Ciência, Tecnologia, Inovações e Comunicações (Brazil), and Korea Astronomy and Space Science Institute (Republic of Korea).

This paper includes data gathered with FIRE at the 6.5 m Magellan Baade Telescopes located at Las Campanas Observatory.

We acknowledge the use of the DELS, DES, VHS, and UKIDSS, UHS, and WISE data.

Facilities: HST (WFC3, ACS), Magellan:Baade (FIRE), Gemini:Gillett (GNIRS), ALMA, NTT (SOFI), PS1 (GPC1), UKIRT, WISE, ESO:VISTA.

Software: Astropy (Astropy Collaboration et al. 2013, 2018), Lmfit (Newville et al. 2019), APLpy (Robitaille & Bressert 2012; Robitaille 2019), spectral-cube (Robitaille et al. 2016), SciPy (Virtanen et al. 2020).

Appendix A
Spectroscopically Rejected Candidates

The spectroscopically rejected candidates that we found in our follow-ups are reported. We adopted the International Astronomical Union naming convention for these sources, which is "PSO JRRR.rrrr+DD.dddd," where RRR.rrrr and +DD.dddd are the R.A. and decl. in decimal degrees (J2000), respectively. The names, PS1 z-band magnitudes ($z_{\rm PS1}$), PS1 y-band magnitudes ($y_{\rm PS1}$), and VHS J-band magnitudes ($J_{\rm VHS}$) are reported in Table A1. An accurate spectral classification of the sources is beyond the scope of this work.

Table A1
Spectroscopic Rejected of Candidates Which are Definitely Not $z > 6$ Quasars

Name	$z_{\rm PS1}$	$y_{\rm PS1}$	$J_{\rm VHS}$
PSO J065.5314−13.3353	22.06 ± 0.18	20.54 ± 0.11	20.54 ± 0.16
PSO J134.2027−07.1366	22.03 ± 0.26	20.30 ± 0.09	19.73 ± 0.10
PSO J123.0135−01.9006	21.93 ± 0.19	20.44 ± 0.10	19.96 ± 0.19
PSO J002.1774−02.9102	22.83 ± 0.30	21.06 ± 0.13	20.19 ± 0.15
PSO J303.7815−00.4066	22.01 ± 0.15	20.49 ± 0.10	19.97 ± 0.13

Appendix B
PSO J344.1442–02.7664: A New Quasar at Redshift ∼6.5

We report the discovery of PSO J344.1442–02.7664, the second quasar that we found within the PS1, DELS, and unWISE catalogs. The *J*-band NIR photometry of this object was obtained using NTT/SofI (Moorwood et al. 1998) with an exposure time of 15 minutes on 2019 July 16. The data were reduced using standard procedures (see Bañados et al. 2014 for details). Then, we did low-resolution NIR spectroscopic follow-up using the 6.5 m Magellan/FIRE on 2019 August 9. The quasar was observed for 10 minutes in high-throughput prism mode ($R = 500$) using a $0\farcs6$ slit width. This in principle gives us an $R = 500$ spectral resolution with a wavelength coverage of 0.82–2.51 μm. The photometric data and the SED fitting results can be seen in Figure 15. On the other hand, Figure 16 shows the two-dimensional spectrum where we estimated the redshift of $z \sim 6.5$ based on a strong Lyα break around the observed-frame wavelength of 9100 Å. The current low-resolution spectrum is not sufficient to calculate accurate emission line and black hole properties for this particular object. Hence, the detailed analysis will be reported in our next paper (Andika et al., in preparation).

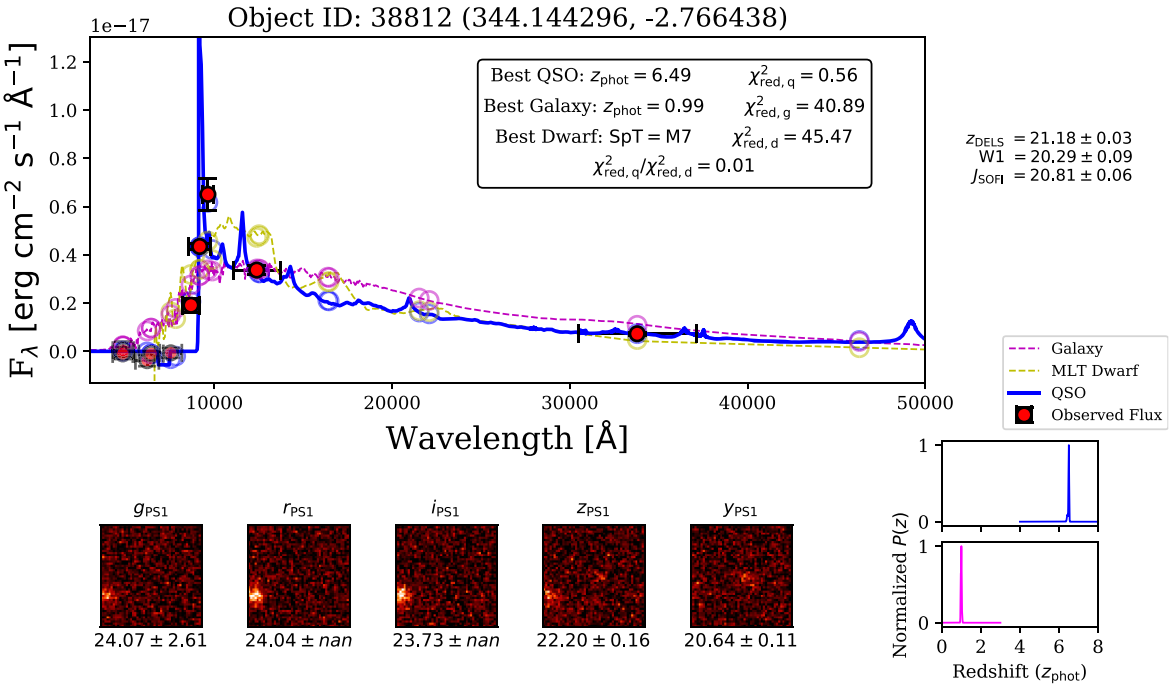

Figure 15. SED fitting result for PSO J344.1442–02.7664. Photometry data are shown with red filled circles with error bars in the top panel. The best-fit quasar spectral template is shown with the blue line and blue circles for model photometry. The same goes for galaxy (magenta) and MLT dwarf models (yellow). The bottom panels show the $12''$ cutouts in the five PS1 bandpasses. All written magnitudes are corrected for Galactic extinction. Finally, the bottom-right panel shows the probability density function (PDF) of the calculated photo-z's for quasar (blue line) and galaxy (magenta line) models.

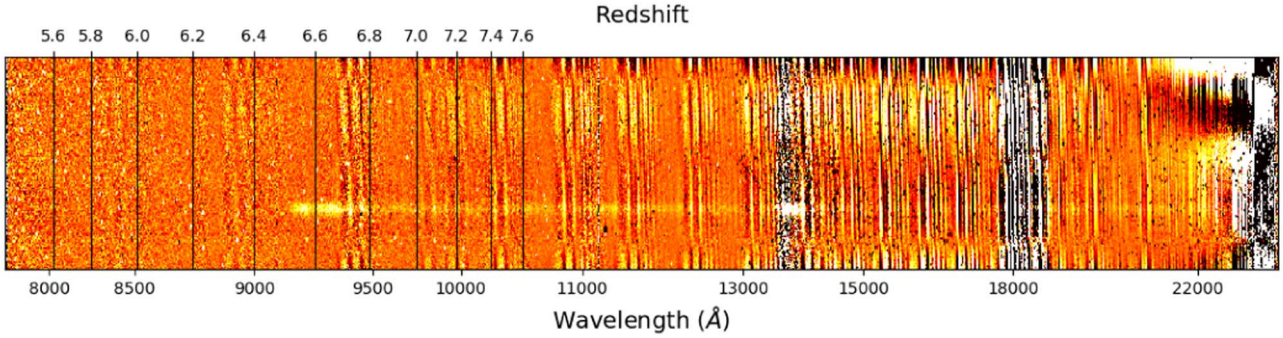

Figure 16. Two-dimensional spectrum of PSO J344.1442–02.7664 obtained with Magellan/FIRE. A strong Lyα break is clearly seen around the observed-frame wavelength of 9100 Å, which means that the Lyα emission is redshifted to $z \sim 6.5$.

ORCID iDs

Irham Taufik Andika https://orcid.org/0000-0001-6102-9526
Knud Jahnke https://orcid.org/0000-0003-3804-2137
Masafusa Onoue https://orcid.org/0000-0003-2984-6803
Eduardo Bañados https://orcid.org/0000-0002-2931-7824
Chiara Mazzucchelli https://orcid.org/0000-0002-5941-5214
Mladen Novak https://orcid.org/0000-0001-8695-825X
Anna-Christina Eilers https://orcid.org/0000-0003-2895-6218
Bram P. Venemans https://orcid.org/0000-0001-9024-8322
Jan-Torge Schindler https://orcid.org/0000-0002-4544-8242
Fabian Walter https://orcid.org/0000-0003-4793-7880
Marcel Neeleman https://orcid.org/0000-0002-9838-8191
Robert A. Simcoe https://orcid.org/0000-0003-3769-9559
Roberto Decarli https://orcid.org/0000-0002-2662-8803
Emanuele Paolo Farina https://orcid.org/0000-0002-6822-2254
Victor Marian https://orcid.org/0000-0003-1733-9281
Antonio Pensabene https://orcid.org/0000-0001-9815-4953
Thomas M. Cooper https://orcid.org/0000-0003-4063-5126
Alejandra F. Rojas https://orcid.org/0000-0003-0006-8681

References

Astropy Collaboration, Price-Whelan, A. M., Sipőcz, B. M., et al. 2018, AJ, 156, 18
Astropy Collaboration, Robitaille, T. P., Tollerud, E. J., et al. 2013, A&A, 558, A33
Abbott, T. M. C., Abdalla, F. B., Allam, S., et al. 2018, ApJS, 239, 18
Bañados, E., Decarli, R., Walter, F., et al. 2015, ApJL, 805, L8
Bañados, E., Rauch, M., Decarli, R., et al. 2019, ApJ, 885, 59
Bañados, E., Venemans, B. P., Decarli, R., et al. 2016, ApJS, 227, 11
Bañados, E., Venemans, B. P., Mazzucchelli, C., et al. 2018, Natur, 553, 473
Bañados, E., Venemans, B. P., Morganson, E., et al. 2014, AJ, 148, 14
Becker, G. D., Bolton, J. S., Madau, P., et al. 2015, MNRAS, 447, 3402
Beelen, A., Cox, P., Benford, D. J., et al. 2006, ApJ, 642, 694
Begelman, M. C., Volonteri, M., & Rees, M. J. 2006, MNRAS, 370, 289
Best, W. M. J., Magnier, E. A., Liu, M. C., et al. 2018, ApJS, 234, 1
Bosman, S. E. I., Becker, G. D., Haehnelt, M. G., et al. 2017, MNRAS, 470, 1919
Bradley, L., Sipőcz, B., Robitaille, T., et al. 2019, astropy/photutils: v0.6, Zenodo, doi:10.5281/zenodo.2533376
Brammer, G. B., van Dokkum, P. G., & Coppi, P. 2008, ApJ, 686, 1503
Brown, M. J. I., Moustakas, J., Smith, J. D. T., et al. 2014, ApJS, 212, 18
Burgasser, A. J. 2014, ASInC, 11, 7
Calzetti, D., Armus, L., Bohlin, R. C., et al. 2000, ApJ, 533, 682
Carilli, C. L., & Walter, F. 2013, ARA&A, 51, 105
Carnall, A. C., McLure, R. J., Dunlop, J. S., & Davé, R. 2018, MNRAS, 480, 4379
Carrasco Kind, M., & Brunner, R. J. 2013, MNRAS, 432, 1483
Chambers, K. C., Magnier, E. A., Metcalfe, N., et al. 2016, arXiv:1612.05560
Chen, S.-F. S., Simcoe, R. A., Torrey, P., et al. 2017, ApJ, 850, 188
Comerford, J. M., Haiman, Z., & Schaye, J. 2002, ApJ, 580, 63
da Cunha, E., Groves, B., Walter, F., et al. 2013, ApJ, 766, 13
Davies, F. B., Furlanetto, S. R., & McQuinn, M. 2016, MNRAS, 457, 3006
Davies, F. B., Hennawi, J. F., & Eilers, A.-C. 2019, ApJL, 884, L19
Davies, F. B., Hennawi, J. F., & Eilers, A.-C. 2020, MNRAS, 493, 1330
Dayal, P., Rossi, E. M., Shiralilou, B., et al. 2019, MNRAS, 486, 2336
De Looze, I., Cormier, D., Lebouteiller, V., et al. 2014, A&A, 568, A62
De Rosa, G., Decarli, R., Walter, F., et al. 2011, ApJ, 739, 56
De Rosa, G., Venemans, B. P., Decarli, R., et al. 2014, ApJ, 790, 145
Decarli, R., Walter, F., Venemans, B. P., et al. 2018, ApJ, 854, 97
Dey, A., Schlegel, D. J., Lang, D., et al. 2019, AJ, 157, 168
Diamond-Stanic, A. M., Fan, X., Brandt, W. N., et al. 2009, ApJ, 699, 782
DiPompeo, M. A., Hickox, R. C., Myers, A. D., & Geach, J. E. 2017, MNRAS, 464, 3526
D'Odorico, V., Feruglio, C., Ferrara, A., et al. 2018, ApJL, 863, L29
Dunne, L., Eales, S. A., & Edmunds, M. G. 2003, MNRAS, 341, 589
Dye, S., Lawrence, A., Read, M. A., et al. 2018, MNRAS, 473, 5113
Eilers, A.-C., Davies, F. B., Hennawi, J. F., et al. 2017, ApJ, 840, 24
Eilers, A.-C., Hennawi, J. F., & Davies, F. B. 2018, ApJ, 867, 30
Eilers, A.-C., Hennawi, J. F., Decarli, R., et al. 2020, arXiv:2002.01811
Fan, X., Strauss, M. A., Becker, R. H., et al. 2006, AJ, 132, 117
Fan, X., Wang, F., Yang, J., et al. 2019, ApJL, 870, L11
Farina, E. P., Arrigoni-Battaia, F., Costa, T., et al. 2019, ApJ, 887, 196
Ferrara, A., Salvadori, S., Yue, B., & Schleicher, D. 2014, MNRAS, 443, 2410
Fitzpatrick, E. L. 1999, PASP, 111, 63
Flesch, E. W. 2019, arXiv:1912.05614
Fujimoto, S., Oguri, M., Nagao, T., Izumi, T., & Ouchi, M. 2020, ApJ, 891, 64
Gordon, K. D., Fouesneau, M., Arab, H., et al. 2016, ApJ, 826, 104
Gould, A. 1995, ApJ, 455, 37
Green, G. M., Schlafly, E., Zucker, C., Speagle, J. S., & Finkbeiner, D. 2019, ApJ, 887, 93
Gunn, J. E., & Peterson, B. A. 1965, ApJ, 142, 1633
Guo, H., Shen, Y., & Wang, S. 2018, PyQSOFit: Python Code to Fit the Spectrum of Quasars, Astrophysics Source Code Library, ascl:1809.008
Habouzit, M., Volonteri, M., Latif, M., Dubois, Y., & Peirani, S. 2016, MNRAS, 463, 529
Harris, D. W., Jensen, T. W., Suzuki, N., et al. 2016, AJ, 151, 155
Helou, G., Khan, I. R., Malek, L., & Boehmer, L. 1988, ApJS, 68, 151
Hopkins, P. F., Hernquist, L., Cox, T. J., et al. 2005, ApJ, 630, 705
Hopkins, P. F., Hernquist, L., Cox, T. J., & Kereš, D. 2008, ApJS, 175, 356
Hryniewicz, K., Czerny, B., Nikołajuk, M., & Kuraszkiewicz, J. 2010, MNRAS, 404, 2028
Inayoshi, K., Haiman, Z., & Ostriker, J. P. 2016, MNRAS, 459, 3738
Inayoshi, K., Visbal, E., & Haiman, Z. 2019, arXiv:1911.05791
Inoue, A. K., Shimizu, I., Iwata, I., & Tanaka, M. 2014, MNRAS, 442, 1805
Jensen, T. W., Vivek, M., Dawson, K. S., et al. 2016, ApJ, 833, 199
Jiang, L., Fan, X., Vestergaard, M., et al. 2007, AJ, 134, 1150
Jiang, L., McGreer, I. D., Fan, X., et al. 2016, ApJ, 833, 222
Kausch, W., Noll, S., Smette, A., et al. 2015, A&A, 576, A78
Kelson, D. D. 2003, PASP, 115, 688
Kennicutt, R. C., & Evans, N. J. 2012, ARA&A, 50, 531
Kumar, P., Chand, H., Srianand, R., et al. 2018, MNRAS, 479, 5075
Laor, A., & Davis, S. W. 2011, MNRAS, 417, 681
Lawrence, A., Warren, S. J., Almaini, O., et al. 2007, MNRAS, 379, 1599
Leighly, K. M., Halpern, J. P., Jenkins, E. B., et al. 2007a, ApJ, 663, 103
Leighly, K. M., Halpern, J. P., Jenkins, E. B., & Casebeer, D. 2007b, ApJS, 173, 1
Liu, Y., & Zhang, S. N. 2011, ApJL, 728, L44
Luo, B., Brandt, W. N., Hall, P. B., et al. 2015, ApJ, 805, 122
Maiolino, R., & Mannucci, F. 2019, A&ARv, 27, 3
Marculewicz, M., & Nikolajuk, M. 2019, arXiv:1910.06175
Matsuoka, Y., Iwasawa, K., Onoue, M., et al. 2018a, ApJS, 237, 5
Matsuoka, Y., Onoue, M., Kashikawa, N., et al. 2016, ApJ, 828, 26
Matsuoka, Y., Onoue, M., Kashikawa, N., et al. 2018b, PASJ, 70, S35
Mazzucchelli, C., Bañados, E., Venemans, B. P., et al. 2017, ApJ, 849, 91
McMahon, R. G., Banerji, M., Gonzalez, E., et al. 2013, Msngr, 154, 35
McMullin, J. P., Waters, B., Schiebel, D., Young, W., & Golap, K. 2007, in ASP Conf. Ser. 376, Astronomical Data Analysis Software and Systems XVI, ed. R. A. Shaw, F. Hill, & D. J. Bell (San Francisco, CA: ASP), 127
Meusinger, H., & Balafkan, N. 2014, A&A, 568, A114
Mitra, K., Chatterjee, S., DiPompeo, M. A., Myers, A. D., & Zheng, Z. 2018, MNRAS, 477, 45
Moorwood, A., Cuby, J. G., & Lidman, C. 1998, Msngr, 91, 9
Mortlock, D. 2016, Quasars as Probes of Cosmological Reionization (Cham: Springer), 187
Mortlock, D. J., Warren, S. J., Venemans, B. P., et al. 2011, Natur, 474, 616
Murphy, E. J., Condon, J. J., Schinnerer, E., et al. 2011, ApJ, 737, 67
Newville, M., Otten, R., Nelson, A., et al. 2019, lmfit/lmfit-py 0.9.14, v0.9.14, Zenodo, doi:10.5281/zenodo.3381550
Ni, Q., Brandt, W. N., Luo, B., et al. 2018, MNRAS, 480, 5184
Nikołajuk, M., & Walter, R. 2012, MNRAS, 420, 2518
Nishizawa, A. J., Hsieh, B.-C., Tanaka, M., & Takata, T. 2020, arXiv:2003.01511
Novak, M., Bañados, E., Decarli, R., et al. 2019, ApJ, 881, 63
Ohsuga, K., Mori, M., Nakamoto, T., & Mineshige, S. 2005, ApJ, 628, 368
Onoue, M., Bañados, E., Mazzucchelli, C., et al. 2020, arXiv:2006.16268
Onoue, M., Kashikawa, N., Matsuoka, Y., et al. 2019, ApJ, 880, 77
Pacucci, F., & Loeb, A. 2019, ApJL, 870, L12
Plotkin, R. M., Shemmer, O., Trakhtenbrot, B., et al. 2015, ApJ, 805, 123
Pons, E., McMahon, R. G., Simcoe, R. A., et al. 2019, MNRAS, 484, 5142

Prochaska, J. X., Hennawi, J. F., Westfall, K. B., et al. 2020, arXiv:2005.06505
Reed, S. L., Banerji, M., Becker, G. D., et al. 2019, MNRAS, 487, 1874
Reed, S. L., McMahon, R. G., Martini, P., et al. 2017, MNRAS, 468, 4702
Richards, G. T., Lacy, M., Storrie-Lombardi, L. J., et al. 2006, ApJS, 166, 470
Robitaille, T. 2019, APLpy v2.0: The Astronomical Plotting Library in Python, Zenodo, doi:10.5281/zenodo.2567476
Robitaille, T., & Bressert, E. 2012, APLpy: Astronomical Plotting Library in Python, Astrophysics Source Code Library, ascl:1208.017
Robitaille, T., Ginsburg, A., Beaumont, C., Leroy, A., & Rosolowsky, E. 2016, Spectral-Cube: Read and Analyze Astrophysical Spectral Data Cubes, Astrophysics Source Code Library, ascl:1609.017
Rousselot, P., Lidman, C., Cuby, J. G., Moreels, G., & Monnet, G. 2000, A&A, 354, 1134
Salviander, S., Shields, G. A., Gebhardt, K., & Bonning, E. W. 2007, ApJ, 662, 131
Sanders, D. B., & Mirabel, I. F. 1996, ARA&A, 34, 749
Sanders, D. B., Soifer, B. T., Elias, J. H., et al. 1988a, ApJ, 325, 74
Sanders, D. B., Soifer, B. T., Elias, J. H., Neugebauer, G., & Matthews, K. 1988b, ApJL, 328, L35
Schauer, A. T. P., Regan, J., Glover, S. C. O., & Klessen, R. S. 2017, MNRAS, 471, 4878
Schlafly, E. F., Meisner, A. M., & Green, G. M. 2019, ApJS, 240, 30
Schneider, P. 2006, Extragalactic Astronomy and Cosmology (Springer)
Selsing, J., Fynbo, J. P. U., Christensen, L., & Krogager, J. K. 2016, A&A, 585, A87
Shakura, N. I., & Sunyaev, R. A. 1973, A&A, 500, 33
Shemmer, O., Brandt, W. N., Schneider, D. P., et al. 2006, ApJ, 644, 86
Shemmer, O., Trakhtenbrot, B., Anderson, S. F., et al. 2010, ApJL, 722, L152
Shen, Y. 2013, BASI, 41, 61
Shen, Y., Richards, G. T., Strauss, M. A., et al. 2011, ApJS, 194, 45
Shen, Y., Wu, J., Jiang, L., et al. 2019, ApJ, 873, 35
Simcoe, R. A., Burgasser, A. J., Schechter, P. L., et al. 2013, PASP, 125, 270
Skrzypek, N., Warren, S. J., Faherty, J. K., et al. 2015, A&A, 574, A78
Smette, A., Sana, H., Noll, S., et al. 2015, A&A, 576, A77
Tanaka, T., & Haiman, Z. 2009, ApJ, 696, 1798
Tang, J.-J., Goto, T., Ohyama, Y., et al. 2019, MNRAS, 484, 2575
Trakhtenbrot, B., Volonteri, M., & Natarajan, P. 2017, ApJL, 836, L1
Tsuzuki, Y., Kawara, K., Yoshii, Y., et al. 2006, ApJ, 650, 57
Venemans, B. P., Bañados, E., Decarli, R., et al. 2015, ApJL, 801, L11
Venemans, B. P., Decarli, R., Walter, F., et al. 2018, ApJ, 866, 159
Venemans, B. P., Findlay, J. R., Sutherland, W. J., et al. 2013, ApJ, 779, 24
Venemans, B. P., McMahon, R. G., Walter, F., et al. 2012, ApJL, 751, L25
Venemans, B. P., Walter, F., Zschaechner, L., et al. 2016, ApJ, 816, 37
Vestergaard, M., & Osmer, P. S. 2009, ApJ, 699, 800
Vestergaard, M., & Wilkes, B. J. 2001, ApJS, 134, 1
Virtanen, P., Gommers, R., Oliphant, T. E., et al. 2020, NatMe, 17, 261
Volonteri, M. 2010, A&ARv, 18, 279
Volonteri, M. 2012, Sci, 337, 544
Volonteri, M., Sikora, M., Lasota, J. P., & Merloni, A. 2013, ApJ, 775, 94
Walter, F., Riechers, D., Cox, P., et al. 2009, Natur, 457, 699
Wang, F., Fan, X., Yang, J., et al. 2017, ApJ, 839, 27
Wang, F., Yang, J., Fan, X., et al. 2019, ApJ, 884, 30
Wang, R., Wagg, J., Carilli, C. L., et al. 2013, ApJ, 773, 44
Wang, R., Wu, X.-B., Neri, R., et al. 2016, ApJ, 830, 53
Willott, C. J., Bergeron, J., & Omont, A. 2015, ApJ, 801, 123
Willott, C. J., Bergeron, J., & Omont, A. 2017, ApJ, 850, 108
Willott, C. J., Delorme, P., Reylé, C., et al. 2010, AJ, 139, 906
Willott, C. J., Omont, A., & Bergeron, J. 2013, ApJ, 770, 13
Wright, E. L., Eisenhardt, P. R. M., Mainzer, A. K., et al. 2010, AJ, 140, 1868
Wu, J., Brandt, W. N., Anderson, S. F., et al. 2012, ApJ, 747, 10
Wu, J., Brandt, W. N., Hall, P. B., et al. 2011, ApJ, 736, 28
Wu, X.-B., Wang, F., Fan, X., et al. 2015, Natur, 518, 512
Wyithe, J. S. B., & Loeb, A. 2002, ApJ, 581, 886
Yang, J., Wang, F., Fan, X., et al. 2019, AJ, 157, 236
Yang, J., Wang, F., Fan, X., et al. 2020, ApJL, 897, L14